# Geophysical Journal International

Royal Astronomical Society

https://doi.org/10.1093/gji/ggaf305

Geophys. J. Int. (2025) 243, 1–20 Advance Access publication 2025 August 7 Research Paper

# Origin of the intensely negative magnetic anomalies in Witwatersrand strata, Vredefort impact structure, South Africa

Iuliia V. Sleptsova<sup>®</sup>, <sup>1</sup> Stuart A. Gilder<sup>®</sup>, <sup>1</sup> Maxime Le Goff, <sup>2</sup> Fabian Dellefant, <sup>1</sup> Claudia A. Trepmann, <sup>1</sup> Florian Lhuillier<sup>®1</sup> and Susan J. Webb<sup>3</sup>

Accepted 2025 August 5. Received 2025 August 1; in original form 2025 January 21

#### SUMMARY

The central portion of the  $2019 \pm 2$  Ma Vredefort (South Africa) impact structure comprises a 40-50 km diameter central uplift of Archean basement rocks surrounded by a 15-20 km wide collar of late Archaean to early Proterozoic Witwatersrand Supergroup sedimentary and volcanic rocks. The collar is characterized by a ring of strongly negative (up to -5500 nT) aeromagnetic anomalies surrounding much of the structure where the strata dip steeply to overturned. To better understand the origin of this magnetic feature, we undertook a ground survey along 20 transects (340 km) in the Vredefort structure using a three-axis fluxgate magnetometer mounted on a mountain bicycle. Upward continuation of our profiles to 150 m matches the aeromagnetic data in shape and amplitude. From the bicycle measurements, we pinpointed the rocks responsible for the extremely negative anomalies. Field observations and microfabric analyses of the rocks from six outcrops substantiated that the magnetic signal correlates with 10-100 m thick metamorphosed banded iron formations (BIFs) at the base of the supergroup as the main producer of the anomalies. Paleomagnetic samples collected from the rocks at the surface that produce the most intense anomalies (up to  $-22\,000$ nT) have extremely high natural remanent magnetization intensities (up to >1000 Am<sup>-1</sup>) likely arising from lightning strikes. Stepwise demagnetization and rock magnetic experiments establish a new protocol to distinguish samples that escaped remagnetization from lightning and possess the established 2.02 Ga paleodirection at Vredefort. From a suite of thermoremanent magnetization (TRM) experiments, the best estimate for the paleofield intensity at the time of impact was 52  $\mu$ T, corresponding to an average remanence of 32.5 Am<sup>-1</sup>. The results of the TRM experiments together with the paleodirection enabled us to successfully model the prominent negative anomalies in the metasediments only when accounting for the postimpact orientation of the BIFs. We interpret the strongly negative magnetic anomalies in the collar region as being formed directly after crater exhumation and uplift of the rocks. This interpretation implies that Bushveld-related metamorphism at 2.06 Ga created the up to mmsized magnetite and garnet crystals in the BIFs, which resided at temperatures higher than the Curie temperature of magnetite (580 °C) until the impact rapidly brought the BIFs close to the surface, where magnetite cooled to acquire a thermal remanence in the 2.02 Ga field.

**Key words:** Magnetic properties; Magnetic anomalies: modelling and interpretation; Palaeomagnetism; Rock and mineral magnetism; Impact phenomena.

# 1. INTRODUCTION

The 2.02 Ga Vredefort structure in South Africa is one of the oldest and largest impact structures on Earth—the original diameter of the crater has been estimated to extend up to 300 km based

on geophysical modelling (Henkel & Reimold 1998), numerical simulations (Allen *et al.* 2022) and the spatial distribution of shockmetamorphic features (Therriault *et al.* 1997a; Grieve & Therriault 2000; Wieland *et al.* 2006). Its geological significance lies not only in its immense scale but also in the unique features and insights it

<sup>&</sup>lt;sup>1</sup>Department of Earth and Environmental Sciences, Ludwig—Maximilians—Universität München, Munich 80333, Germany. E-mail: iu.sleptsova@lmu.de, gilder@lmu.de

<sup>&</sup>lt;sup>2</sup>Institut de Physique du Globe de Paris, Paris F-75005, France

<sup>&</sup>lt;sup>3</sup>School of Geosciences, University of the Witwatersrand, Johannesburg 2000, South Africa

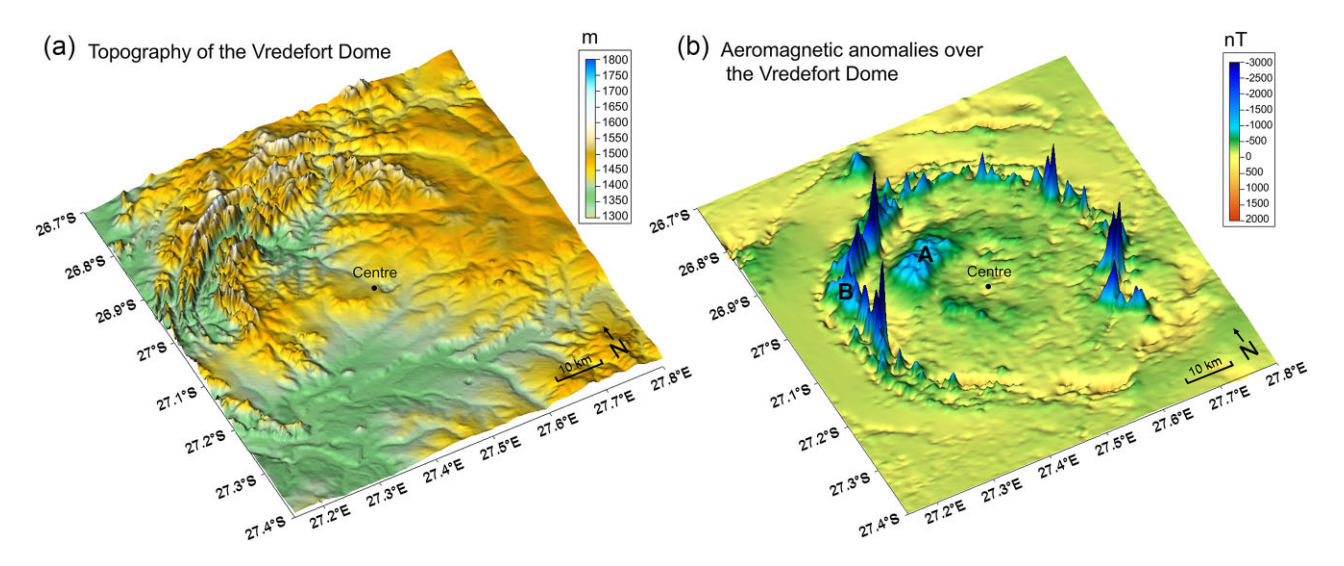


Figure 1. (a) Topography of the Vredefort Dome based on a Shuttle Radar Topography Mission (SRTM) digital elevation model (DEM); vertical scale in meters exaggerated  $\sim$ 500x. (b) Aeromagnetic anomalies over the Vredefort Dome based on Council for Geosciences aeromagnetic data; the vertical scale (in nT) is inverted, with negative anomalies shown as relief: A—a 'horseshoe-shaped' region of prominent negative anomalies within the basement rocks, B—a ring of prominent negative anomalies surrounding the basement rocks. Both modified after Carporzen (2006).

offers into Earth's ancient history (Tredoux *et al.* 1999; Moser *et al.* 2001; Hart *et al.* 2004). The remains of the impact crater, called the Vredefort Dome, comprise a  $\sim$ 40 km wide flat central region of Archean basement rocks surrounded by a semicircular  $\sim$ 20 km wide rim of late Archaean to early Proterozoic sedimentary and volcanic units that form a topographic high due to the resistant, steeply dipping quartzites in the Witwatersrand Basin collar sediments (Figs 1 and 2).

Aeromagnetic data acquired 150 m above the surface reveal two distinct, semicircular, intensely negative anomalies (Fig. 1b; Stettler et al. 1999). Toward the structure's centre within the 3.0-3.5 Ga crystalline basement rocks lies a 'horseshoe-shaped' region of prominent negative anomalies, reaching up to -3000 nT (A in Fig. 1b). Investigations by Hart et al. (2000) and Carporzen et al. (2005) revealed exceptionally high, randomly oriented natural remanent magnetizations (NRMs) and high Q ratios (ratios of remanent to induced magnetization) in the Archean rocks, later attributed to a lightning-induced magnetization (Carporzen et al. 2012; Salminen et al. 2013). Muundjua et al. (2007) suggested a relationship between the 'horseshoe-shaped' magnetic feature and the amphibolite to granulite metamorphic facies transition exposed in the basement floor. They proposed that impact-related thermal and shock metamorphism at this transition zone could be related to the focusing and defocusing of shock waves at a rheologic interface during impact, which created an enhanced thermoremanent magnetization (TRM), thereby accounting for the large anomaly. More recently, Dellefant et al. (2022) suggested that impact-related fracturing of coarse-grained magnetite, together with fine-grained magnetite exsolutions within ilmenite that formed during impact, increased the remanent magnetization of the host rock, which together contribute to the negative, 'horseshoe-shaped' magnetic anomaly when magnetite cooled through its Curie temperature (580 °C) upon crater exhumation.

The origin and characteristics of the outer concentric magnetic feature (B in Fig. 1b), which exhibits even stronger negative anomalies (up to -5500 nT) than the inner 'horseshoe-shaped' region, remain unresolved. Corner *et al.* (1990) attributed this feature to 'ferruginous shales' of the West Rand Group within the 2.7 Ga metasediments in the sedimentary collar. Other magnetic models

explained the anomaly by invoking broad (up to 1 km), coherently magnetized sources with remanence directions similar to those of the impact melt dykes (Jackson 1982; Henkel & Reimold 1998, 2002). However, based on garnet-biotite thermometry, Gibson et al. (1998) estimated post-impact temperatures in the lower West Rand Group to be  $\sim$ 500–525 °C, a result corroborated by numerical models of Turtle et al. (2003) and Ivanov (2005). The West Rand Group includes iron-rich units (banded iron formations) such as the Water Tower Slates and Contorted Beds, which are known to produce strong magnetic anomalies elsewhere in the Witwatersrand Basin (Krahmann 1936; Roux 1970; Frimmel 1996; Smith et al. 2013; Tucker et al. 2016). Despite the known association of iron-rich formations with strong magnetic anomalies, until now, no study has directly documented the magnetic properties of the specific lithologies within the Vredefort collar that produce the negative anomalies in the sedimentary collar of the Vredefort Dome.

To address this problem, we undertook a high-resolution ground magnetic survey throughout the Vredefort Dome using a three-axis fluxgate magnetometer mounted on a bicycle, covering about 340 km along 20 profiles that cross the sedimentary collar into the structure's interior. From the magnetometer data, we located the surface outcrops producing the strong magnetic signals and then collected oriented samples. This study presents the results of the paleo- and rock magnetic experiments and the microfabric analysis of the surface samples, together with forward modelling of the ground magnetic field data, to elucidate the origin of the magnetic anomalies in the collar and the geological implications.

## 2. GEOLOGICAL SETTING

## 2.1. Geology of the Vredefort Dome

The Vredefort Dome is an exposed remnant of the original impact crater formed by a meteorite impact at  $2019 \pm 2$  Ma (Spray 1995; Kamo *et al.* 1996; Moser 1997). It is located within the Witwatersrand Basin (27.05°S, 27.48°E) in the central Kaapvaal Craton (South Africa), 120 km southwest of Johannesburg. Two

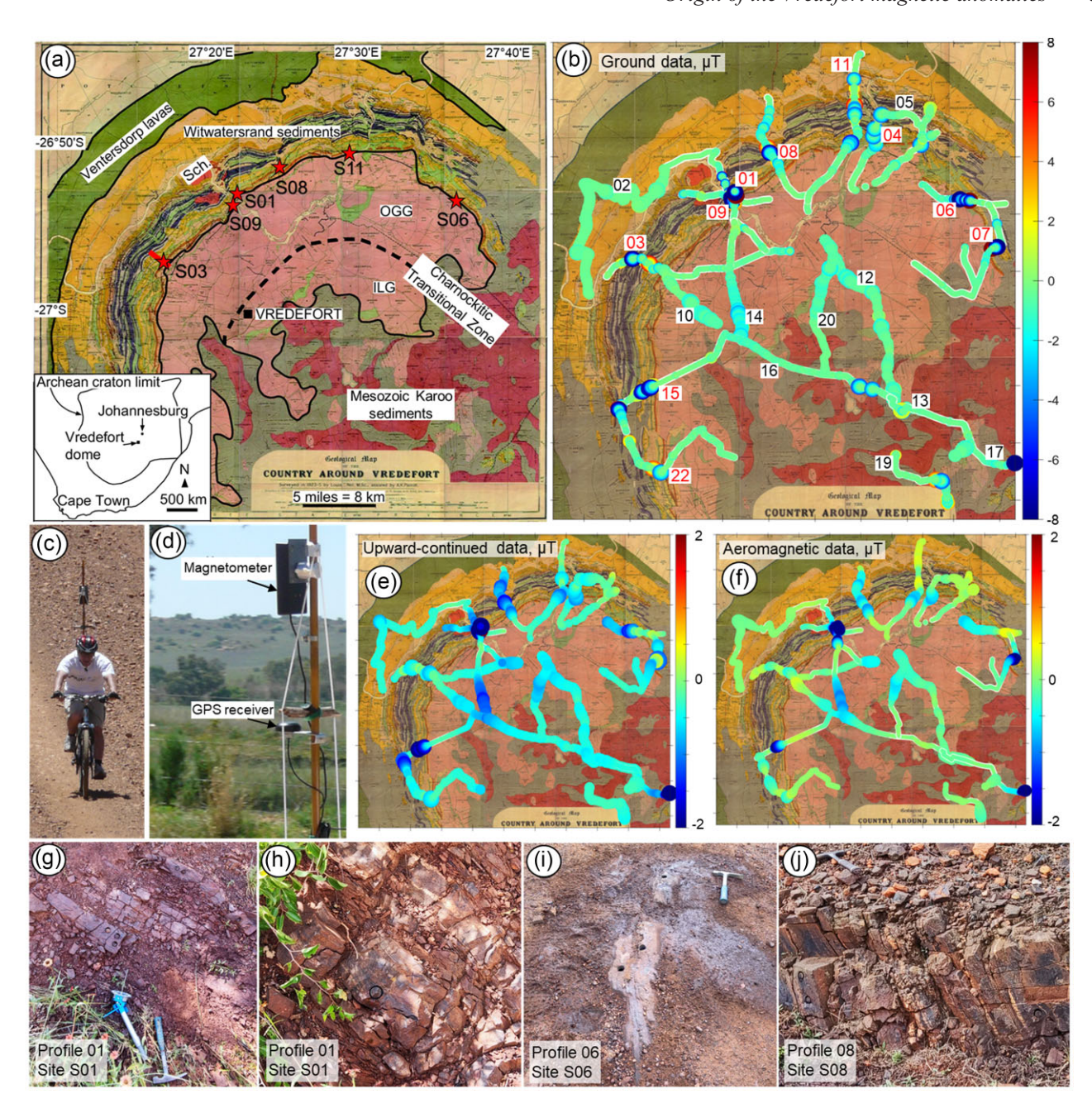


Figure 2. (a) Simplified geological map of the Vredefort Dome (modified after Nel 1927). We specifically used Nel (1927) since it is the original source used in more modern maps. Red stars mark paleomagnetic sampling sites collected at the intensely negative magnetic anomalies identified from bicycle-mounted magnetometer profiles; OGG = outer granite gneiss, ILG = Inlandsee leucogranofels, Sch. = Schurwedraai alkaline-granite body. The thick red line near S03 represents the position of the Hospital Hill Subgroup lithostratigraphic column shown in Fig. 4(a). (b) Ground magnetic profiles superimposed on the geological map. Profile numbers are labelled, with those crossing the contact between the Witwatersrand sediments and basement rocks in red (scale in  $\mu$ T). (c) Field photo of the mountain bicycle with mounted fluxgate magnetometer and GPS receiver. (d) Close-up of the three-axis fluxgate magnetometer and GPS receiver. (e) Ground magnetic data upwards-continued to 150 m altitude for comparison with (f) aeromagnetic data interpolated to the same spacing as the ground data. (g-j) Field photos of paleomagnetic sampling sites: (g, h) site S01, (i) site S06 and (j) site S08. Geological hammer shown for scale; paleomagnetic core diameters are 2.54 cm.

billion years' worth of erosion has reduced the size of the structure to its current  $\sim$ 80 km diameter as defined by the steeply dipping collar sediments (Schreyer 1983; Huber *et al.* 2023; Fig. 2a). Impact melting is evidenced through the presence of granophyre dykes, which are thought to have been injected into the basement from above (Koeberl *et al.* 1996; Therriault *et al.* 1997b; Huber *et al.* 2022; Fourie *et al.* 2023; Reimold *et al.* 2023). Pseudotachylites

are ubiquitous (e.g. Gibson & Reimold 2005; Reimold & Gibson 2006). Shock features are variably overprinted by annealing, which increases in intensity toward the centre of the dome (Schreyer 1983; Reimold & Gibson 2006). Based on these features, within 5 km of the centre, maximum shock pressures exceeded 30–35 GPa, and locally more than 45 GPa, decreasing to  $\sim$ 10 GPa 20 km from the centre (Gibson & Reimold 2005).

Exhumation following the impact and subsequent erosion, estimated to be 7-11 km from geobarometric analyses (Schreyer 1983; Gibson et al. 1998) and geophysical considerations (Henkel & Reimold 1998), have exposed a steeply dipping cross-section of the middle and lower crust (Hart et al. 1990a, 2004; Lana et al. 2003a). Within the central region, the crystalline basement comprises a complex, high-grade metamorphic terrane dominated by Archean migmatitic gneisses (Lana et al. 2003a, b, 2004). Traditionally, the basement rocks have been divided into amphibolite-facies granitic gneisses (outer granite gneiss, OGG) and granulite-facies granofels (Inlandsee leucogranofels, ILG), as well as charnockitic gneisses (Charnockitic Transitional Zone) (Fig. 2a; Hart et al. 1981, 1990a). The rocks in the innermost part of the structure are poor in magnetite (Hart et al. 1995; Carporzen et al. 2005), which explains the lack of significant magnetic anomalies there (Fig. 1). This part also contains limited outcrops of ultramafic rocks from the upper mantle (Hart et al. 1990b).

The collar rocks comprise a ~20-km-thick section of unconformity-bounded sedimentary and volcanic sequences deposited between 3.07 and 2.25 Ga in the Witwatersrand Basin (Clendenin et al. 1988; Beukes et al. 2024). They have undergone substantial deformation, dipping up to 120° (overturned), during the impact event (e.g. Bisschoff 1988; Jahn & Riller 2009) that created the semicircular mountain chain defining the Vredefort Dome (Figs 1a and 2a). The collar strata dip 30°-60° south-eastwards in the southeastern sector, as observed in boreholes (Antoine et al. 1990; Brink et al. 1997; Lana et al. 2003b). The oldest rocks in the collar are 3.07 Ga Dominion Group (Armstrong et al. 1991) metavolcanic rocks, followed by 2.9 to 2.7 Ga sedimentary rocks of the Witwatersrand Supergroup: a lower sequence of pelitic, quartzite and ironstone units (West Rand Group, ~4 km thick), and an upper sequence dominated by quartzitic conglomerate (Central Rand Group,  $\sim$ 3 km thick) that hosts gold deposits (Tucker *et al.* 2016). Ventersdorp Supergroup volcanism at 2.7 Ga marks the termination of sedimentation in the Witwatersrand Supergroup (Armstrong et al. 1991), after which the Transvaal Supergroup began accumulating at  $\sim$ 2.6 Ga when a shallow sea covered much of the Kaapvaal Craton. Deposition within the Transvaal Supergroup terminated at approximately 2.25 Ga (Clendenin et al. 1988; Walraven 1997). The collar rocks also contain numerous igneous intrusions, most of which are related to the Ventersdorp (2.7–2.6 Ga) and Bushveld Complex (2.06–2.05 Ga) events (Bisschoff 1969, 1972). Much of the southeastern part of the structure is covered by Late Palaeozoic to Jurassic Karoo Supergroup sedimentary rocks (Bisschoff 1988; Fig. 2a).

The collar rocks display variable metamorphic grades, increasing from lower greenschist facies in the outer parts to amphibolite facies within the inner collar (Bisschoff 1982; Schrever 1983; Gibson & Stevens 1998). The cause of this pattern has been ascribed to a regional event that affected the entire Witwatersrand Basin related to 2.05-2.06 Ga Bushveld intrusions, 40 Myr before the impact (Gibson 1993; Gibson & Wallmach 1995). This is supported by <sup>40</sup>Ar/<sup>39</sup>Ar dating of the metamorphic assemblages (Gibson et al. 2000) and the existence of alkali granite and associated ultramafic-mafic intrusions (e.g. Schurwedraai, Lindequesdrift, Roodekraal) in the Vredefort collar rocks that have SHRIMP zircon ages of 2052  $\pm$  14 Ga equivalent to that of the Bushveld magmatic event at ca. 2060 Ma (Graham et al. 2005). Based on pressure-temperature estimates, Gibson & Wallmach (1995) concluded that the peak geothermal gradient reached ~40 °C km<sup>-1</sup> during this event. The peak metamorphic temperatures of the inner collar rocks were constrained to 570-600 °C, based on the presence of mid-amphibolite-facies pre-impact porphyroblastic assemblages in metapelites of the lower Witwatersrand Supergroup (Gibson & Wallmach 1995; Gibson & Stevens 1998).

#### 2.2. Magnetic anomalies related to the collar sediments

A kilometre-scale ring of strongly negative (up to -5500 nT) aeromagnetic anomalies encompassing the crystalline basement rocks (B in Fig. 1b) has been loosely ascribed to ferruginous shales belonging to the West Rand Group, which forms the basal part of the Witwatersrand Supergroup (Corner et al. 1990; Fig. 2a). The West Rand Group of the Witwatersrand Supergroup extends approximately four kilometres in thickness and comprises marine shelf mudstone and quartzite with interbedded banded iron formations (BIFs), which are commonly referred to as 'magnetic shales' (Frimmel 1996; Smith et al. 2013). Magnetic surveys by Krahmann (1936) identified nine magnetic anomalies attributed to magnetic shale bands within the West Rand Group in the Witwatersrand Basin. Major anomalies (>1000 nT) were associated with the Water Tower Slates, the Contorted Bed and the West Rand shales, which are widespread throughout the basin. All three iron formations are sufficiently magnetic to be detected at depths of several hundred meters and serve as magnetic markers that help locate the gold-bearing strata of the Central Rand Group (Roux 1970; Tucker et al. 2016). The Water Tower Slates BIF lies in the lower part of the Parktown Formation, usually 100 to 150 m above the basal Orange Grove Quartzite (orange marker bed in Fig. 2a), and its thickness generally ranges between 9 and 30 m. The Contorted Bed BIF is generally 600 m above the Water Tower Slates and has a thickness of 10-50 m (Smith et al. 2013; Beukes et al. 2024). The polarity, shape and degree of resolution of the anomalies associated with the BIFs depend on the magnetic properties of the beds, the bedding attitudes, and the depth below the observation level. For instance, an aeromagnetic profile flown at a height of  $\sim$ 275 m across southerly dipping Witwatersrand beds over the eastern suburbs of Johannesburg showed positive anomalies with a maximum intensity of ~800 nT, whereas an aeromagnetic profile at a height of ~610 m across overturned Lower Witwatersrand beds striking north-northeast 19 km south of Ventersdorp (~90 km northwest of Vredefort) showed negative anomalies with ∼600 nT amplitudes (Roux 1970).

The prominent negative magnetic anomalies in the collar are mainly absent in the southeast (Fig. 1b). In the southeastern sector of the Vredefort Dome, where the collar strata dip 30°-60° SE (e.g. Antoine *et al.* 1990; Brink *et al.* 1997; Lana *et al.* 2003b), magnetic anomalies are strongly positive (up to +1 500 nT; Fig. 1b). Geophysical data and limited borehole information from this sector suggest a complicated structure beneath the Karoo Supergroup cover rocks (e.g. Corner *et al.* 1990; Martini 1992; Molezzi *et al.* 2019). In this region, the Witwatersrand Supergroup appears thinner, around 7.5 km compared to 9.5 km in the northwest (e.g. Antoine *et al.* 1990; Brink *et al.* 1997; Lana *et al.* 2003b).

# 3. METHODS

#### 3.1. Magnetic survey

The Geological Survey of South Africa conducted an aeromagnetic survey over the Vredefort Dome in 1977 (Fig. 1b; Corner & Wilsher 1989; Stettler *et al.* 1999). Total field data were collected

along north–south flight lines with a terrain clearance of 150 m, a 240 km h<sup>-1</sup> speed, and a sampling interval of one second; flight line spacing was 1 km. Perpendicular tie lines were flown every 10 km. The data were converted into a 500 m grid using a cubic spline method (Corner & Wilsher 1989). The relationship between the aeromagnetic data and the complex geology of the sedimentary collar is poorly resolved due to the aeromagnetic data's low resolution, except along flight lines.

To acquire higher-resolution magnetic data, we conducted ground-based measurements along 20 magnetic profiles spanning the Vredefort Dome (Fig. 2b). An Applied Physics Systems 1540S fluxgate magnetometer was mounted on a bicycle (Figs 2c and d),  $\sim$ 2 m above the ground surface, with X, Y and Z magnetic field components recorded simultaneously at 0.3-s intervals. This method allowed for spatial separation between measurement points from 0.5 to 3 m depending on the bicycle's velocity. A GPS receiver (RoyalTek RGM/REB-21R; Fig. 2d), positioned 45 cm below the fluxgate sensors, simultaneously recorded geographic positions with an accuracy of about 10 m. Tests conducted to assess the potential magnetic interference from the GPS and the bicycle determined that their influence did not exceed 50 nT.

To minimize the effects of variations in sensor orientation and height when cycling on uneven terrain, we calculated the total magnetic field intensity from the three-component magnetometer data. Diurnal variations were corrected using measurements from the closest INTERMAGNET Observatory (Hartebeesthoek, HBK: 25.88°S, 27.71°E), which ranged from 20 to 60 nT  $d^{-1}$ . The total field averaged 28 432 nT, consistent with the International Geomagnetic Reference Field (IGRF) intensity of 28 161 nT (Alken et al. 2021). The total magnetic field intensity measured at HBK was subtracted from each profile to derive the magnetic anomalies. The sources of artificial magnetic anomalies were primarily limited to the transient passage of motor vehicles. Localized artificial anomalies were distinguishable from geological signals by their spatial distribution and frequency characteristics. These disturbances were effectively mitigated during data processing, which involved smoothing (1.3 s  $\approx$  7 points), removing outliers using a Hampel filter, and ignoring some data obtained when cycling at speeds <5 km h<sup>-1</sup> to ensure consistency and reliability of the datasets. Minor uncertainties may remain within ±50 nT, which are insignificant compared to the amplitude of the measured anomalies. Upward continuation of the magnetic profiles was calculated using a MAT-LAB code based on the FORTRAN program by Gibert & Galdeano (1985) to an altitude of 150 m.

#### 3.2. Paleomagnetic and rock magnetic studies

Based on the ground magnetic survey, we conducted field investigations in the areas with the most pronounced negative magnetic anomalies to ascertain the geological context relative to the magnetic signatures. We used the geological map by Nel (1927) in the field (Fig. 2a) and found it to be remarkably accurate, particularly for the metasedimentary collar, whose stratigraphy remains largely unchanged in modern maps (e.g. Bisschoff 2000). Six surface outcrops of metasediments were identified along six of the magnetic profiles (Figs 2a and b; Table 1). A battery-powered drill was used to collect 57 one-inch-diameter cores. Each core was oriented using magnetic and sun compass measurements. Magnetic declination varied from  $-135^{\circ}$  to  $126^{\circ}$  with a median value of  $-15.5^{\circ} \pm 65.1^{\circ}$  (IGRF declination  $= -20.2^{\circ}$ , Alken et~al.~2021).

All experiments were performed at Ludwig-Maximilians-Universität (LMU, Munich). Stepwise demagnetization experiments were performed in a magnetically shielded room (~500 nT) on 115 cylindrical specimens, normally using two specimens from a single core, 8 mm in diameter. Alternating field (AF) demagnetization up to peak fields of 90 mT was carried out using the automated SushiBar system (Wack & Gilder 2012), which incorporates a threeaxis, 2G Enterprises Inc., superconducting magnetometer to measure magnetic moments up to  $5 \times 10^{-5}$  Am<sup>2</sup>, as well as a fluxgate magnetometer to measure higher magnetic moments (Kaub et al. 2023). AF demagnetization up to peak fields of 150 mT was carried out on 50 specimens using a D-Tech, D-2000 demagnetizer. Lowfrequency susceptibility (465 Hz) was measured with a Bartington Instruments MS2B sensor. Remanent magnetization directions were determined with principal component analysis (Kirschvink 1980); mean directions were calculated using Fisher statistics (Fisher 1953). Hysteresis loops, backfield isothermal remanent magnetization curves and thermomagnetic curves were measured using a Petersen Instruments variable field translation balance (5 mm-diameter cylinders).

TRM experiments were performed using an ASC Scientific TD-48 oven on 41 specimens previously subjected to AF demagnetization so the samples' original NRM intensities and susceptibilities were known. TRMs were measured using an AGICO JR-6 spinner magnetometer. First, a magnetic field of 20 µT was applied during cooling from 700 °C to room temperature (TRM<sub>20</sub>), susceptibility was measured  $(X_{20})$ , then a second TRM on the same samples was imparted using 40 µT (TRM<sub>40</sub>), whereafter susceptibility was again measured (X<sub>40</sub>). Stepwise thermal demagnetization was performed on eight specimens from site S03 that acquired a TRM<sub>40</sub> from the second TRM acquisition experiment and on eight 'fresh' specimens (5 mm-diameter cylinders) carrying NRM from sister samples. To further investigate the nature of the NRM, we imparted an artificial TRM using an applied field of 52  $\mu$ T on 13 specimens (5 mm-diameter cylinders) during cooling from 600 °C to room temperature. We then performed stepwise AF demagnetization up to 120 mT peak fields using a three-axis, 2G Enterprises Inc., superconducting magnetometer with an in-line AF-coil.

#### 3.3. Microscopy

Polished, uncovered thin sections (ca. 25 µm; Fig. S5, Supporting Information) were prepared from 10 paleomagnetic cores from site S01 (samples V2203, V2206, V2211), site S09 (samples V2216, V2221), site S03 (samples V2226, V2235), site S06 (sample V2237), site S11 (sample V2248) and site S08 (sample V2260) then investigated by polarization microscopy (Leica DM2700 P) using both transmitted and reflected light. Photomicrographs were taken with a Leica MC170 HD camera and processed with the Leica Application Suite X 3.08.19082 software. Samples V2216, V2221 (site S09) and V2235 (site S03) were studied with a Hitachi SU5000 scanning electron microscope (SEM) equipped with a field emission gun, energy-dispersive X-ray spectroscopy (EDS) detector (Oxford Instruments), backscattered electron (BSE) detector, and NordlysNano high-sensitivity EBSD detector (Oxford Instruments). SEM observations were conducted using accelerating voltages of 20 kV and working distances of 10-25 mm. In situ micro-Raman spectroscopy was carried out with a HORIBA JOBIN YVON XploRa ONE micro-Raman system at the Munich Mineralogical State Collection. Details on the methodology are identical to those described in Dellefant et al. (2022).

Downloaded from https://academic.oup.com/gji/article/243/1/ggaf305/8225764 by guest on 08 September 2025

Table 1. Parameters of ground magnetic profiles and corresponding paleomagnetic sites from the sedimentary collar of the Vredefort Dome.

Profile		DipDir (°)	Dip (°)	Azimuth (°)	$\operatorname{Int}_{\operatorname{Min}}\left(\operatorname{nT}\right)$	Lat <sub>Min</sub> (°S)	Lon <sub>Min</sub> (°E)		FWHM (m)			
01		162	123	145	-21 930	26.88089	27.363 42	3 42	06			
03		288	65	104	-10520	26.93928	27.25261	261	21			
9		0	78	24	-4735	26.83211	27.51350	3.50	50			
90		40	102	96	-15900	26.88711	27.60700	7 00	7			
07		270	110	223	-13100	26.92881	27.64739	739	20			
80		150	113	151	9068-	26.84639	27.40119	119	21			
60		155	86	149	-16380	26.88839	27.36069	69 (	42			
11		150	06	214	-6234	26.83772	27.48883	3 83	36			
15		105	130	64	-9105	27.05161	27.272 42	2.42	47			
22		270	80	99	-4698	27.12581	27.28319	3 1 9	89			
Site	Lat (°S)	Lon (°E)	NNRM/TRM	$NRM (A m^{-1})$	$TRM_{20} (A m^{-1})$	$TRM_{40} (A m^{-1})$	X <sub>NRM</sub> (SI)	$X_{20}$ (SI)	X <sub>NRM</sub> /X <sub>20</sub>	X <sub>20</sub> /X <sub>40</sub>	Q-value	NRM/TRM40
S01	26.88122	27.36342	28/8	184 ± 176	15 ± 10	25 ± 19	$0.17 \pm 0.18$	$0.22 \pm 0.17$	$1.2 \pm 0.1$	$1.2 \pm 0.2$	57 ± 64	$20 \pm 22$
S03	26.94711	27.28 100	24/8	$11 \pm 7$	$3.3 \pm 1.6$	$7.2 \pm 3.7$	$0.03 \pm 0.04$	$0.024 \pm 0.036$	$1.3 \pm 0.2$	$0.9 \pm 0.1$	$42 \pm 25$	$1.3 \pm 0.4$
90S	26.88714	27.60753	12/6	$1013 \pm 810$	$31 \pm 22$	$57 \pm 38$	$0.30 \pm 0.18$	$0.31 \pm 0.19$	$0.8 \pm 0.2$	$1.0 \pm 0.1$	$135 \pm 94$	$22 \pm 25$
808	26.85 522	27.40964	16/6	$148 \pm 144$	$9.1 \pm 3.1$	$17 \pm 4$	$0.27 \pm 0.14$	$0.21 \pm 0.10$	$1.3 \pm 0.1$	$1.2 \pm 0.1$	$23 \pm 13$	$9\pm 5$
60S	26.89042	27.36206	23/8	$625 \pm 656$	$19 \pm 6$	$35 \pm 14$	$0.27 \pm 0.14$	$0.29 \pm 0.10$	$1.0 \pm 0.2$	$1.1 \pm 0.1$	$103 \pm 101$	$21 \pm 15$
S11	26.84128	27.48472	14/5	$3.8 \pm 1.4$	$5.3 \pm 2.8$	9 ± 5	$0.05 \pm 0.02$	$0.046 \pm 0.018$	$1.2 \pm 0.2$	$1.2 \pm 0.1$	$3.2 \pm 0.8$	$0.4 \pm 0.2$

Abbreviations: Upper part—Magnetic survey information: DipDir and Dip, dip direction and dip angle of the strata near the contact between the sedimentary collar and the basement core measured in the field longitude of Int<sub>Min</sub>; FWHM, full width at half maximum of Int<sub>Min</sub>. Lower part—Paleomagnetic and rock magnetic information: Lat and Lon, latitude and longitude of the sampling site; N, number of measured specimens for the natural remanent magnetization (NRM) and the thermoremanent magnetization (TRM); all values reported as the average  $\pm$  single standard deviation; TRM20 and TRM40, lab imparted TRMs Q-value, ratio of natural remanent magnetization (NRM) to induced magnetization assuming the ambient field of  $H = 22.7 \text{ A m}^{-1}$ ; NRM/TRM40, ratio of NRM to TRM40, values >>1 or <<1 likely indicate or read from the geological map (Nel 1927); Azimuth was measured over a two-km-long part of the profile used for modelling; Int<sub>Min</sub>, most negative value of the magnetic anomaly; Lat<sub>Min</sub> and Long<sub>Min</sub>, latitude and in applied magnetic fields of 20 and 40  $\mu$ T, respectively; X<sub>NRM</sub>, bulk magnetic susceptibility (SI units); X<sub>20</sub> and X<sub>40</sub>, bulk magnetic susceptibility measured after acquisition of TRM<sub>20</sub> and TRM<sub>40</sub>, respectively; overprinting by lightning.

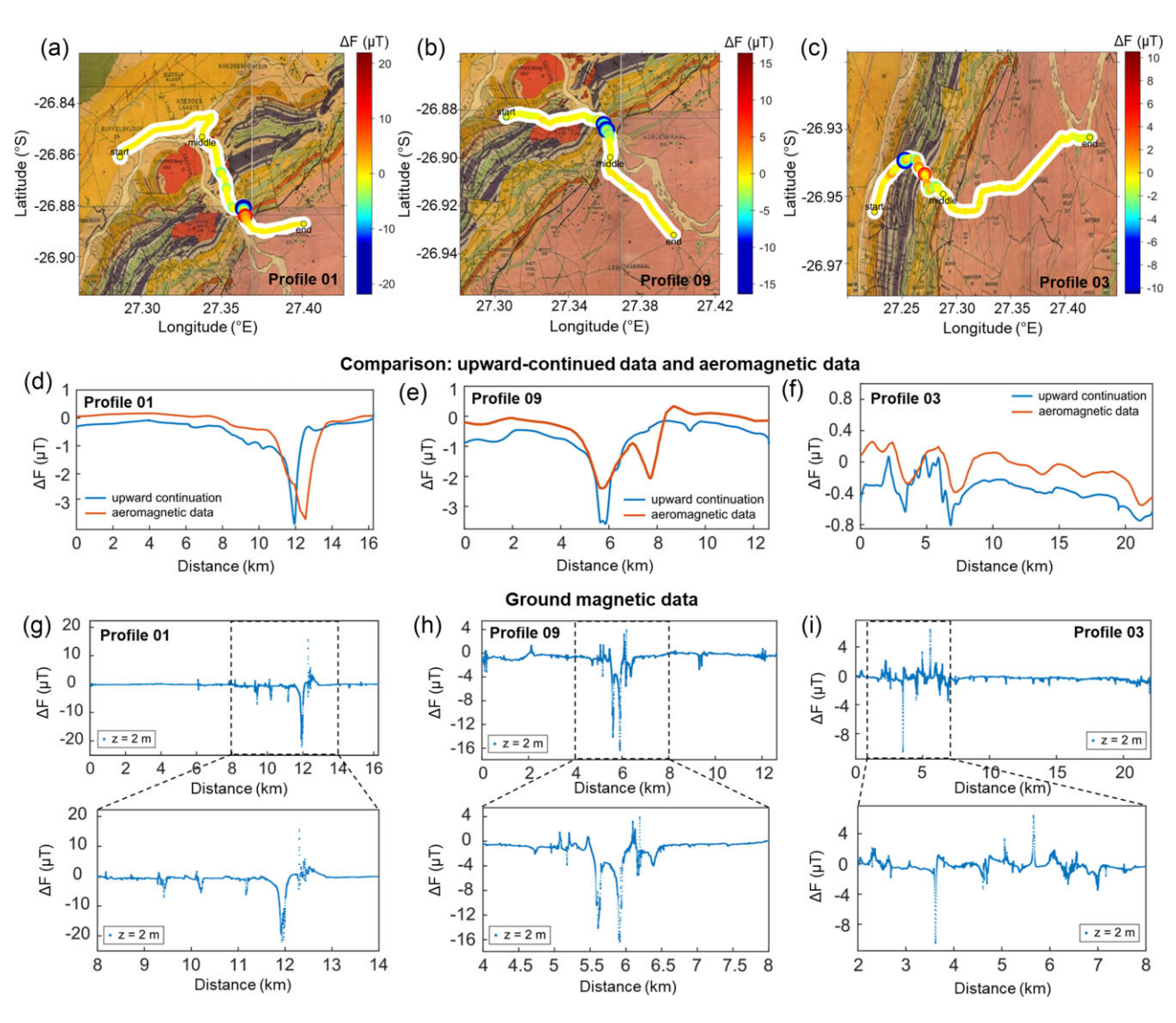


Figure 3. (a-c) Ground magnetic data for three profiles (01, 09 and 03) superimposed on the geological map (modified after Nel 1927); (d-f) comparison between upward-continued data to 150 m (in blue) and projected aeromagnetic data (in orange); (g-i) ground magnetic data.

# 3.4. Modelling magnetic anomalies

We modelled the magnetic anomalies in the Vredefort collar metasediments along 10 two-kilometre-long segments of the profiles proximal to the contact between the sedimentary rocks and the basement core by averaging data every 10 m. GRAVMAG software was used for forward modelling (Pedley et al. 1993; updated by Jones 2012), which creates source structures from polygons in the X–Z plane. Each source body was assigned the same remanent magnetization direction ( $D = 25.0^{\circ}$ ,  $I = 57.2^{\circ}$ ) as the impact-generated granophyre dykes (Carporzen et al. 2005) and the same magnetic susceptibility (0.1 SI) for the contribution of induced magnetization. Structural constraints used bedding data (Table 1) from our field observations or from the geological map by Nel (1927) for the top part of the source bodies. We interactively modified the shape of the bodies at depth to better fit the observed magnetic data. As the beds dip steeply to overturned, they must become less steep and eventually flatten, going away from the Vredefort structure. With few exceptions, the source bodies were modelled to depths of 500 m, as greater depths did not significantly affect the output. For example, for profile 01, changing the base depth of magnetic bodies to 1000 m increased the amplitude of the magnetic anomaly by only 3 per cent.

# 4. RESULTS

# 4.1. Magnetic survey

The ground magnetic survey data revealed significant variations in magnetic field intensity, with the largest anomalies observed in the northwestern segment of the collar (Figs 2b and 3). Minimum and maximum anomalies are  $-21\,930$  nT to  $+\,24\,050$  nT, respectively, which, to put in perspective, are roughly double the present field intensity in both a positive and negative sense. We used a scale of  $\pm 8000$  nT in Fig. 2(b) to better visualize the anomalies. Each ground profile within the collar sediments is characterized by the most pronounced negative anomalies in the vicinity of the contact between the sedimentary strata and the basement floor. The

full width at half maximum (FWHM in Table 1) of the negative anomalies ranged from 7 to 90 m, with an average of 36.5 m.

The upward continued data from our profiles to an altitude of 150 m (Fig. 2e) mostly matched the relative shape and amplitude of the gridded aeromagnetic data, which were interpolated to the same spacing as the ground data (Fig. 2f). Although the major anomaly patterns are comparable, some systematic offsets in baseline levels, particularly in regions of weak anomalies, are noticeable, as commonly attributed to survey and processing discrepancies. These differences likely result from the distinct processing workflows applied to the original aeromagnetic data set, including regional detrending, levelling and filtering. Figs 3(d)–(f) compare the upward continued bicycle data to 150 m altitude (blue curve) with the aeromagnetic data (orange curve) by projecting both onto a straight line (Fig. 1b; Corner & Wilsher 1989; Stettler et al. 1999). Both curves match in amplitude for profile 01; however, the negative anomaly in the aeromagnetic data has a larger FWHM and is located closer to the collar-core contact than in the upward-continued data. The aeromagnetic data for profile 09 have two negative anomalies, while the upward-continued data have only one with a higher amplitude. For profile 03, both upward-continued and aeromagnetic data match in shape, however, the upward-continued data include short wavelength variations and have magnetic anomalies farther from the collar-core contact.

For other profiles (Fig. S6, Supporting Information), the upward-continued data mostly match the aeromagnetic data. The differences in shape, amplitude, and shifts in the positions of the magnetic peaks of up to 1 km (Figs 3d–f and Fig. S6, Supporting Information) can be explained by the fact that the ground data were recorded at much higher spatial resolution (from 0.5 to 3 m) than the aeromagnetic survey (1 km) and were better referenced to the geographic coordinate system. Additionally, minor spatial mismatches can be attributed to the issues of projecting the inherently curvilinear data onto a straight line. This simplification, necessary for comparative plotting, does not account for local curvature or terrain-following deviations along the actual measurement profiles, thereby introducing positional offsets when compared to gridded aeromagnetic data.

Our ground magnetic survey indicates that the most negative anomalies lie less than 2 km from the base of the Witwatersrand system (Figs 2b and 4b, c). When more than one anomaly exists in a profile, the amplitude diminishes with distance from the contact (Fig. 4b). After summing all ground profiles and comparing the sum against the generalized lithostratigraphic column, the most distinct magnetic signatures correspond to the Water Tower Slates and the Contorted Bed within the Parktown Formation (Fig. 4). These two BIFs are laterally persistent in the Witwatersrand Basin and are interpreted as having been deposited in a marine environment (McCarthy 2006; Smith *et al.* 2013).

# 4.2. Stepwise demagnetization

NRM intensities of 115 specimens ranged from 1.5 to 2438 A m<sup>-1</sup>, with a median of 68 A m<sup>-1</sup>; susceptibilities are likewise spread over three orders of magnitude, from 0.0028 to 0.8209 SI. The samples exhibited high Q-ratios [ratios of the NRM to the magnetization induced by the Earth's magnetic field {22.7 A m<sup>-1</sup> (Koenigsberger 1938)}], ranging from 2 to 307 with a median of 35 (Table 1).

Fig. 5 illustrates representative orthogonal projections and normalized magnetization decay plots. Most samples exhibit low median destructive fields (MDF), with a median of 11 mT, with >90

per cent of the original remanence removed by 90 mT. AF demagnetization to 150 mT removed only 11–73 per cent of the original magnetization for four samples from site S01 (Fig. 5a). Demagnetization trajectories often follow great circle paths that might or might not reach a stable endpoint, prohibiting principal component analysis (Figs 5a–e). For example, taking a single demagnetization direction of the 40 mT step reveals a large scatter for each sample within each site except for samples from site S03 (Fig. 6).

In contrast, stepwise AF demagnetization of all 12 samples from site S03 isolated a linear component that decays univectorially to the origin on orthogonal projections (Figs 5f–i). The magnetization directions of the samples within each of the four individual blocks from site S03 are highly coherent from block to block (Fig. 6c; Table S1, Supporting Information). The directions of the blocks are close to the direction of the geomagnetic field determined from granophyre dykes emplaced during impact ( $D=25^{\circ}$ ,  $I=57.2^{\circ}$ ,  $\alpha_{95}=3.9^{\circ}$ ; Carporzen *et al.* 2005). Jackson (1982) sampled the Contorted Bed and found high-NRM intensities (92.5  $\pm$  28.3 A m<sup>-1</sup>) and a magnetization direction of  $D=33^{\circ}$  and  $I=48^{\circ}$  ( $\alpha_{95}=8.7^{\circ}$ , N=8 samples).

## 4.3. Rock magnetism

Most samples lie along the single domain (SD) to multidomain (MD) mixing curve for pure magnetite (Dunlop 2002). Samples V2234 and V2235 from block #4 of site S03 are the most enriched in SD grains of the four blocks from the site (Fig. 7a); block #4 also contains remanence directions most resembling those of the granophyre dykes. Strong-field (220 mT) thermomagnetic curves (Figs 7b—e and Fig. S1, Supporting Information) indicate Curie temperatures between 552 and 580 °C, likely from Ti-poor titanomagnetite. Deflections around 300–350 °C and lower magnetizations during cooling than heating (Figs 7c and d) suggest the presence of maghemite, which then alters to hematite upon heating. Three samples exhibited weak deflections around 680 °C, indicative of hematite (Fig. 7c; Figs S1c and j, Supporting Information).

## 4.4. Thermal remanent magnetization experiments

Here we discuss the results from the TRM experiments that imparted magnetic fields of 20 and 40  $\mu$ T. TRM<sub>20</sub> intensities acquired in an applied magnetic field of 20  $\mu$ T ranged from 1.4 to 69.3 A m<sup>-1</sup>, with an average of 13.7 A m<sup>-1</sup>, while TRM<sub>40</sub> intensities acquired in fields of 40  $\mu$ T ranged from 2.8 to 123.4 A m<sup>-1</sup>, with an average of 25.0 A m<sup>-1</sup>. On average, susceptibility decreased 15 per cent after the first heating (X<sub>20</sub>/X<sub>NRM</sub> = 0.85) and 10 per cent after the second heating (X<sub>40</sub>/X<sub>20</sub> = 0.90), which should be considered when comparing the NRM, TRM<sub>20</sub> and TRM<sub>40</sub> data (Table 1). On average, TRM<sub>40</sub>/TRM<sub>20</sub> is 1.9—close to a factor of two, as expected, since both values are lightning-independent. NRM/TRM<sub>40</sub> is much higher than 1 for four sites (18  $\pm$  18, N = 28), with site S11 being much lower than 1 (0.4  $\pm$  0.2, N = 5); this is in stark contrast with site S03, whose NRM/TRM<sub>40</sub> is indistinguishable from 1 (1.3  $\pm$  0.4, N = 8) (Table 1).

Thermal demagnetization spectra of NRM and TRM<sub>40</sub> were sometimes discrepant (Fig. S3, Supporting Information), likely due to alteration during heating. Changes in low-field susceptibility measured after each heating step indicated that the potential alteration in magnetic mineralogy started around 450 °C in most of the samples (Fig. S3, Supporting Information). The demagnetization spectra of the NRMs of site S03 closely resembled the demagnetization spectra of the artificial TRMs, suggesting that the natural

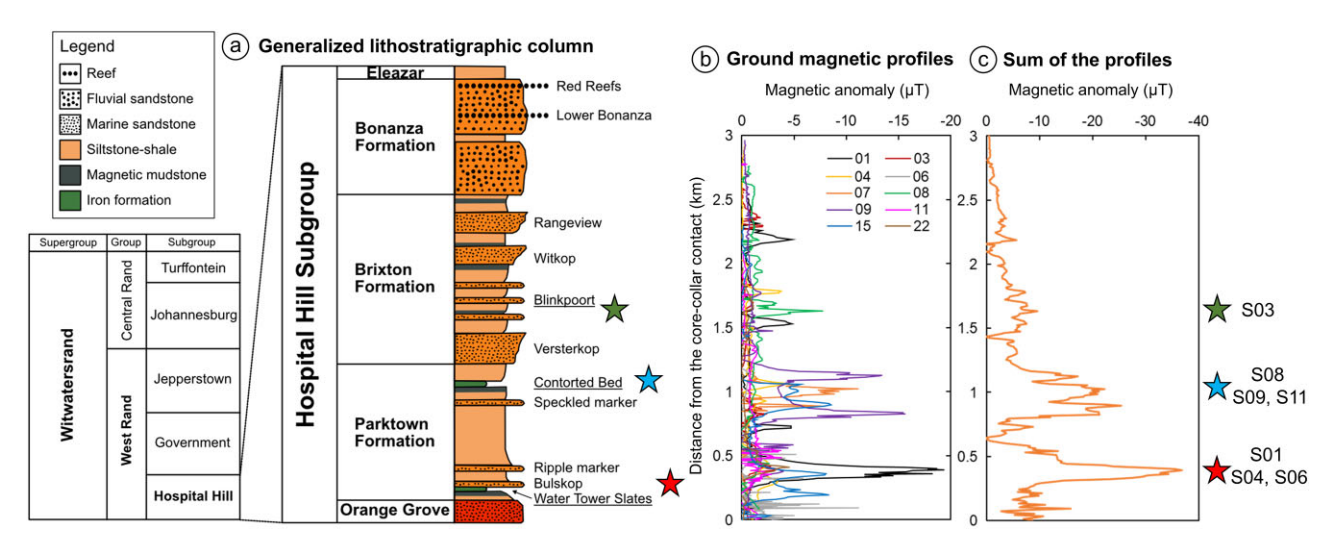


**Figure 4.** (a) Generalized lithostratigraphic column of the Hospital Hill Subgroup within the West Rand Group of the Witwatersrand Supergroup (modified after Guy *et al.* 2010 and Nel 1927). (b) Stack of ground magnetic profiles with respect to the stratigraphic distance from the sediment-basement contact; (c) sum of the profiles shown in panel (b). Paleomagnetic sites are shown as stars; different colours and positions of the stars indicate the correlation between the stratigraphy and peak magnetic anomalies.

magnetization of site S03 is of thermoremanent origin. If site S03 indeed carries a thermoremanence that has not changed since its acquisition, and considering NRM/TRM<sub>40</sub> = 1.3, the approximate paleointensity estimate is 40  $\mu$ T × 1.3 = 52  $\mu$ T.

# 4.5. Microscopic observations

The Vredefort collar samples divide into three groups (I, II, III) based on their fabric and mineralogy. Groups I and II have magnetite and hematite as rock-forming Fe-minerals (Figs 8a-i) together with quartz, whereas Group III has magnetite and hematite as accessory phases (Figs 8k and 1) with a matrix composed of fine-grained phyllosilicate and quartz grains (Fig. 8j and Figs S4bd, Supporting Information). Group I (samples V2206, V2203 and V2211; site S01) shows a pronounced foliation defined by alternating mm-wide quartz-dominated layers comprising fine-grained limonite and hematite and layers with coarse-grained magnetite, hematite and quartz (Fig. 8a; Figs S5a and b, Supporting Information). Moreover, finely dispersed euhedral magnetite grains with diameters ranging from a few um to 100s of um are often rimmed by hematite, as well as quartz grains with diameters of  $\approx$ 50  $\mu$ m (Figs 8a and b). Rarely, strongly weathered amphiboles (actinolite) occur with lengths of a few 100s of μm. The proportion of silicates to iron-oxides is about equal, albeit variable from layer to layer. This lithologic type corresponds well with the banded iron formations (Contorted Bed and Water Tower Slates) within the Lower Witwatersrand Supergroup described by Smith et al. (2013).

Group II (samples V2216, V2221, V2237, V2248 and V2260; sites S09, S06, S11 and S08) has magnetite and hematite with diameters of a few  $\mu m$  to 100s of  $\mu m$  (Figs 8c–i), like Group I, but Group II has a less-pronounced foliation and higher amphibole contents (Fig. 8c) characterized by acicular to lamellar habits (Fig. S4a, Supporting Information). Amphiboles, having lengths of 100s of  $\mu m$ , are colourless or greenish and have high iron and magnesium contents (EDS: Fig. S8, Supporting Information). Raman analyses indicate a cummingtonite–grunerite solid solution. Euhedral garnets with diameters of 100s of  $\mu m$  have sets of fractures subparallel to each other and at a high angle to the foliation (Figs 8f and g). EDS

analyses yield an average composition of 70 per cent almandine, 10 per cent pyrope, 10 per cent spessartine and 10 per cent grossular. Limonite often associates with garnet, especially within its fractures (Fig. 8h). The samples exhibit variable degrees of alteration, likely due to surficial weathering. The mineral assemblage from Group II agrees with higher greenschist facies conditions (Bischoff 1982).

Group III (samples V2226 and V2235 from site S03) has no apparent foliation and a matrix consisting of a few  $\mu m$ -sized phyllosilicates (biotite and muscovite), quartz, as well as minor garnet (Fig. 8j), which can also occur as grains 100s of  $\mu m$  in diameter, likely formed from the phyllosilicates in the matrix (Fig. S4b, Supporting Information). Unlike Groups I and II, the matrix in Group III samples has no  $\mu m$ -sized magnetite and hematite grains, although magnetite grains with diameters of  $\approx\!50~\mu m$  can occur as an accessory phase (Figs 8k and I). Pyrite, chalcopyrite and ilmenite occur as  $\mu m$  to 100s of  $\mu m$ -sized aggregates with irregular grain boundaries within the matrix (Figs S4c and d, Supporting Information). Group III is similar to a Fe-rich metapelite described by Beaton et~al.~(2022), who attributed the assembly to amphibolite facies conditions.

#### 4.6. Magnetite and hematite microfabrics

Large euhedral magnetite grains with a rim of hematite (Figs 8d and e) result from the oxidation and pseudomorphic replacement of magnetite by hematite, called martitization (Mücke & Raphael Cabral 2005). Within samples V2211 (site S01), V2216 (site S09) and V2260 (site S08), the adjacent matrix of the coarse magnetite grains only consists of quartz and has no  $\mu$ m-sized iron-oxides (Figs 8d and e), which might be due to a metamorphic growth of magnetite at the expense of the surrounding fine-grained iron-oxides. Locally, magnetite grains have garnet inclusions with euhedral shapes (Figs 8g and h), indicating that they formed after the garnets and that garnets could serve as seeds for nucleation and growth.

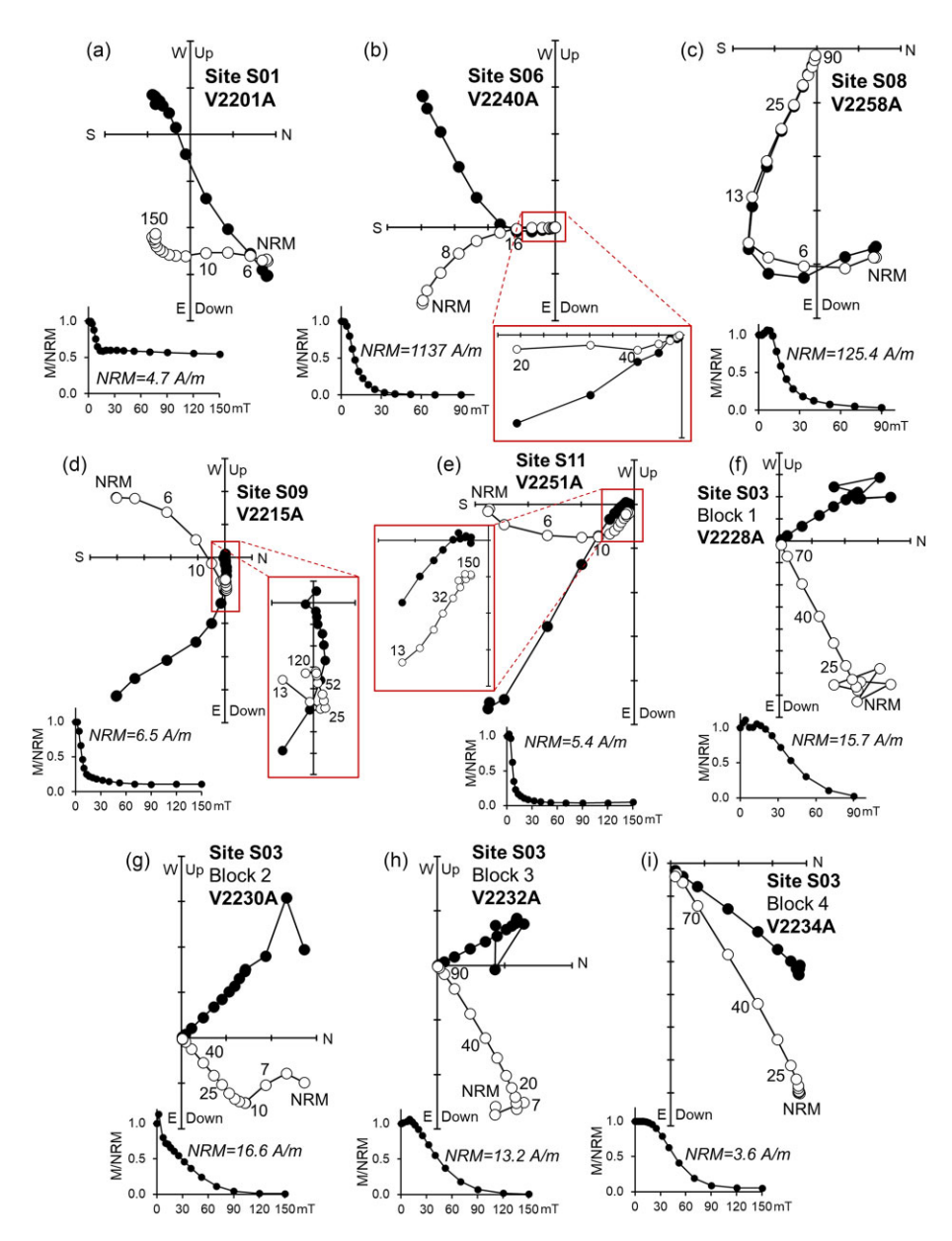


Figure 5. Representative orthogonal projections of stepwise alternating field demagnetization and normalized magnetization decay plots for the Vredefort collar rock samples in geographic coordinates. Open (solid) circles on orthogonal diagrams denote the projection on the vertical (horizontal) plane.

# 4.7. Garnet and quartz microfabrics

Within samples V2216 (site S09) and V2260 (site S08), quartz is enriched in the strain shadows of coarse euhedral magnetite grains, which define the foliation parallel to the layering (Fig. 8c). This is likely the result of the strain-induced dissolution of quartz at shortening sites (normal to the foliation) and its subsequent precipitation at sites of extension/least shortening (stretching lineation within the foliation plane), i.e. dissolution precipitation creep (Wassmann & Stöckhert 2013). Furthermore, the sets of fractures within the garnet of sample V2216 (site S09) are quasi-perpendicular to the apparent foliation (Fig. 8f); thus, brittle deformation causing the parallel fractures might be related to the Bushveld metamorphic event or to impact-induced exhumation.

# 4.8. Modelling the magnetic anomalies

Since the TRM experiments defined the average  $TRM_{40}$  intensity as 25 A m<sup>-1</sup>, and given that NRM/TRM<sub>40</sub> is  $1.3\pm0.4$  for site S03, thought to have escaped lightning effects, the thermoremanence is likely underestimated by 30 per cent, so the intensity of the remanent magnetization was set to 32.5 A m<sup>-1</sup>. Fig. 9 compares three models of the magnetic anomalies to ground magnetic profiles; Fig. S6 (Supporting Information) shows another eight modelled profiles. The largest negative anomalies concentrate in the northwestern sector (Fig. 2b, Table 1). For instance, profile 01 exhibits the strongest anomaly with an amplitude of  $-21\,930$  nT and a FWHM of 90 m (Fig. 9a). Modelling this anomaly involved creating two closely spaced magnetic bodies, each  $\sim$ 70 m thick, positioned less than 10 m apart (Fig. 9a). Although the calculated anomaly matches the

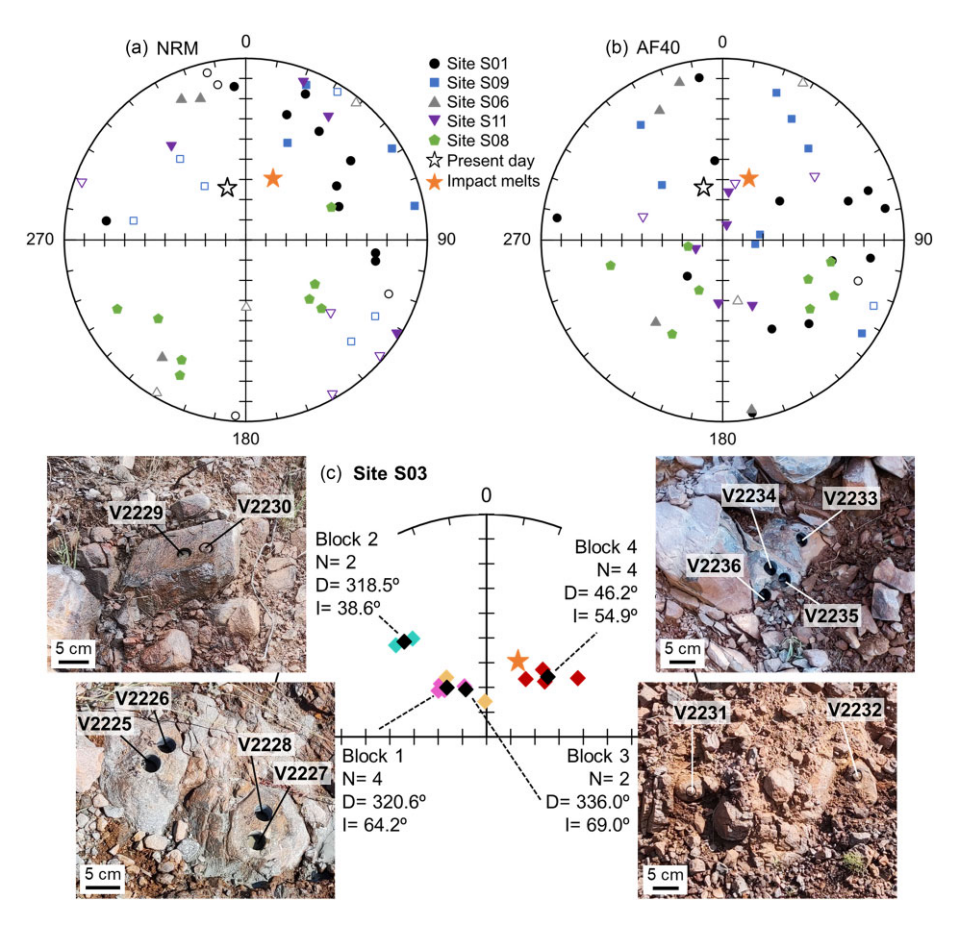


**Figure 6.** Stereographic projection of (a) the NRM directions and (b) the magnetization directions derived from a single demagnetization step at 40 mT determined for 45 samples collected at five paleomagnetic sites from the sedimentary collar of the Vredefort Dome. The orange star indicates the mean paleomagnetic direction of granophyre dykes (Carporzen *et al.* 2005); the black unfilled star indicates the present-day field direction. (c) Stereographic projection of the magnetization directions from site S03, together with field photos of the four blocks collected at the site (sample #s shown). Solid symbols plotted on the lower hemisphere, and unfilled symbols are on the upper hemisphere; mean directions shown in black.

width of the observed anomaly, its amplitude falls short by 7000 nT, indicating a need for higher magnetizations within the bodies to attain the observed amplitudes. Profile 09 contains two major peaks with amplitudes of –14 100 and –15 800 nT and two smaller peaks with amplitudes of –5460 and –2960 nT (Fig. 9b). Modelling these anomalies required the creation of four magnetic bodies of varying thickness, spaced approximately 200–300 m apart. The calculated profile mimics the main features of the data with some exceptions (Fig. 9b). Profiles 15 and 04 (Figs S6a and e, Supporting Information) also require four magnetic bodies, while profiles 22 and 07 (Figs S6b and d, Supporting Information) are modelled with three bodies. TRMs of 32.5 A m<sup>-1</sup> are enough to match the anomaly amplitudes for these profiles.

Site S03, which possesses coherent paleomagnetic directions, was sampled near the negative peak of profile 03 (western sector) with an amplitude of -3520 nT (Fig. 9c). Modelling involved four magnetic bodies with thicknesses up to 30 m, showing good agreement with observed data (Fig. 9c). Profiles 06, 08 and 11 from the northern to the northeastern sector of the dome exhibited similar anomaly shapes characterized by shorter spatial wavelengths (Figs S6c, d and g, Supporting Information). Bodies with thicknesses up to 30 m, closely spaced within 200 m, were created to model these profiles. While the calculated magnetic anomalies in general align well in amplitude with the observed ground data, achieving an exact match in shape remains challenging. In particular, the

long-wavelength component of the negative anomaly in profile 08 could not be reproduced using thin magnetic sources, indicating a limitation of the simplified model geometry in capturing the full complexity of the magnetic sources.

# 5. RELATIONSHIP OF MAGNETIC ANOMALIES TO THERMOREMANENCE

To generate profiles with magnetic parameters across the circular geometry of the impact structure (Fig. 10), we computed the linear distances between each site/sample we collected with respect to the centre of the structure (27.05°S, 27.48°E). To extract the aeromagnetic data, we first calculated a rectangular averaged grid comprised of 805 data points by averaging every 15 nearest corner grid points (Corner & Wilsher 1989; Stettler et al. 1999; Fig. 1b), with the coordinates of the corners of the grid (-27.0988°S, 27.2656°E;  $-26.8435^{\circ}$ S,  $27.2656^{\circ}$ E;  $-27.0988^{\circ}$ S,  $27.6406^{\circ}$ E;  $-26.8435^{\circ}$ S, 27.6406°E). We then computed the linear distance between the averaged grid point and the centre (Fig. 10a). The aeromagnetic profiles exhibited two negative peaks, one with an amplitude up to -1200 nT, approximately 12 km from the centre, and another with an amplitude up to -3200 nT, about 20 km from the centre. The first peak corresponds to the Charnockitic Transitional Zone (Hart et al. 1981; Fig. 2a), while the second one characterizes the Witwatersrand metasediments.

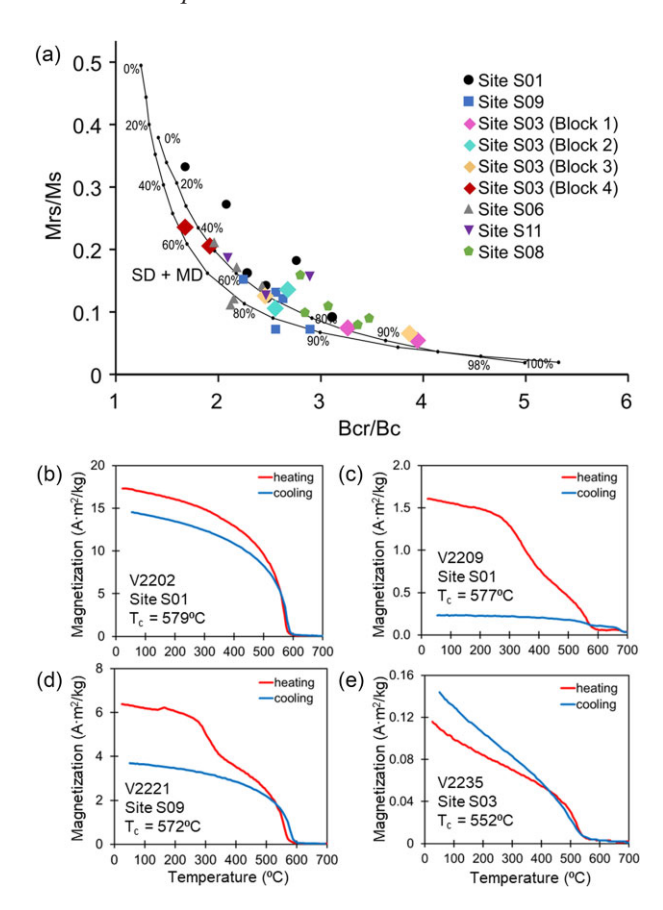


**Figure 7.** (a) Day *et al.* (1977) plot of 33 samples from six paleomagnetic sites of the Vredefort collar rocks. Mrs/Ms refers to the ratio of saturation remanent magnetization (Mrs) to saturation magnetization (Ms), and Bcr/Bc refers to the ratio of coercivity of remanence (Bcr) to coercive force (Bc). Single domain (SD) and multidomain (MD) mixing curves for pure magnetite from Dunlop (2002). (b—e) Representative thermomagnetic curves of selected samples.

To compare the basement rocks with collar metasediments, we performed analogous TRM experiments on 59 samples (5 mmdiameter cylinders; volume =  $1 \times 10^{-7}$  m<sup>3</sup>) of the Archean basement rocks studied by Carporzen et al. (2005) and Carporzen (2006). Intensities in an applied magnetic field of 20 µT (TRM<sub>20</sub>) ranged from 0.04 to 6.9 A m<sup>-1</sup>, with an average of 0.8 A m<sup>-1</sup>, while TRM<sub>40</sub> intensities ranged from 0.1 to 13.6 A m<sup>-1</sup>, with an average of 1.6 A m<sup>-1</sup>—two times greater than in a 20 μT field as expected (Table S2, Supporting Information). TRM<sub>40</sub> versus bulk magnetic susceptibility  $X_{40}$  follow a linear trend for both basement and sedimentary rock types, confirming that a single, predominant magnetic carrier, namely magnetite, is responsible for holding the TRM. The average TRM<sub>40</sub>/X<sub>40</sub> (slope in Fig. 10b) is 134 with a coefficient of determination  $(R^2) = 0.568$  for basement rocks (N = 59) and 144 for sedimentary rocks with  $R^2 = 0.836$  (N = 41), with the combined data set being 144 with  $R^2 = 0.896$  (N = 100).

Fig. 10(c) presents TRM<sub>40</sub> intensities as a function of distance from the centre of the Vredefort structure, with six data points >40 A m<sup>-1</sup> cut off for better scaling. Due to uneven sampling, a direct comparison with the averaged grid data in Fig. 10(a) is limited. A better correlation exists if we extract the aeromagnetic anomaly value above each sample's locality (noting high uncertainty). Fig. 10(d) shows that, between 0 and -1000 nT, the more negative the anomaly, the stronger the TRM<sub>40</sub> intensity. Beyond

-1000 nT, TRM $_{\rm 40}$  values in sedimentary rocks plateau at  $\sim \! 100$  A  $\rm m^{-1}$ , achieving saturation. A robust factor in explaining the amplitude of the aeromagnetic anomaly comes from the saturation magnetization (Ms), which can be considered a proxy for magnetite concentration (Fig. 10e). The correlation is also well evinced when plotting the remanent magnetization after saturation (Mrs) (Fig. 10f). For clarity, Ms and Mrs values were truncated at 5 A  $\rm m^2~kg^{-1}$  (20 out of 33 data points were cut off in Fig. 10e) and 0.5 A  $\rm m^2~kg^{-1}$  (24 out of 34 data points were cut off in Fig. 10f), respectively. The maximum TRM $_{\rm 40}$  intensity in the basement rocks, located  $\sim \! 11$  km from the centre, aligns with the first broad peak of the aeromagnetic data (the 'horseshoe-shaped' anomaly), while the high TRM $_{\rm 40}$  intensities of the metasediments align with the second peak (Figs 10a and c).

#### 6. DISCUSSION

# 6.1. Lightning remagnetization

Paleomagnetic analyses on the Vredefort collar metasediments sampled from regions exhibiting pronounced negative magnetic anomalies reveal remarkably high NRM intensities up to 2438 A m<sup>-1</sup> with Q-values up to 307 (Table 1). Most of the samples collected from the metasediments have low MDF values (median of 11 mT) and exhibit demagnetization trajectories following great circle paths (Figs 5a–e). Carporzen *et al.* (2012) proposed that the high Q-values in basement samples represented the effects of lightning strikes, a widespread phenomenon in South Africa (Christian *et al.* 2003; Gijben 2012). Laboratory experiments by Salminen *et al.* (2013) demonstrated that lightning strikes could indeed produce intense magnetization in the Vredefort basement rocks. Our results show that most of the surface sedimentary rocks were also remagnetized by lightning strikes.

To evaluate the extent of lightning-related overprinting, we compared the stepwise AF demagnetization behaviour of NRM with that of a laboratory-imparted TRM<sub>52</sub>. The comparison revealed two tendencies. For samples from site S03, NRM and TRM decayed in a similar way up until ~30 mT (Figs S2d-g, Supporting Information), whereas the AF demagnetization spectra of NRM and TRM<sub>52</sub> for the nine samples from other sites are completely different in this range (Figs S2a-c, S2h-m, Supporting Information). We quantified these differences using two metrics: (1) (NRM/TRM)<sub>20mT</sub>, by taking the magnetic moment at a particular AF demagnetization step (e.g. 20 mT) and dividing NRM at 20 mT by TRM at 20 mT =  $(NRM/TRM)_{20mT}$ , and  $(2) (\frac{NRM_{20mT}}{NRM})/(\frac{TRM_{20mT}}{TRM})$ , which is denoted  $(NRM/TRM)_{20mT}^{norm}$ , by normalizing each value by the original NRM or TRM. Ratios were calculated for three AF steps at 20, 25 and 30 mT, as well as the corresponding normalized values (Table 2). All ratios (normalized or not) are close to 1 for all four samples from site S03, indicating similar coercivity spectra and minimal or no lightning remagnetization. In contrast, (NRM/TRM)<sub>20 mT</sub>,  $(NRM/TRM)_{25 \text{ mT}}$  and  $(NRM/TRM)_{30 \text{ mT}}$  for nine samples from other sites are > 1.3, while  $(NRM/TRM)_{20mT}^{norm}$ ,  $(NRM/TRM)_{25mT}^{norm}$ and  $(NRM/TRM)_{30mT}^{norm}$  are <<1.0 (ca. 0.2), consistent with the acquisition of lightning-induced isothermal remanent magnetization (Table 2). Hence, NRM/TRM and (NRM/TRM)<sup>norm</sup> ratios can be used to determine whether samples were influenced by lightning: non-normalized values greater than 1.0 and normalized values less than 1.0 can be considered characteristics of lightning strikes, whereas values near 1.0 indicate the absence of lightning-related overprinting.

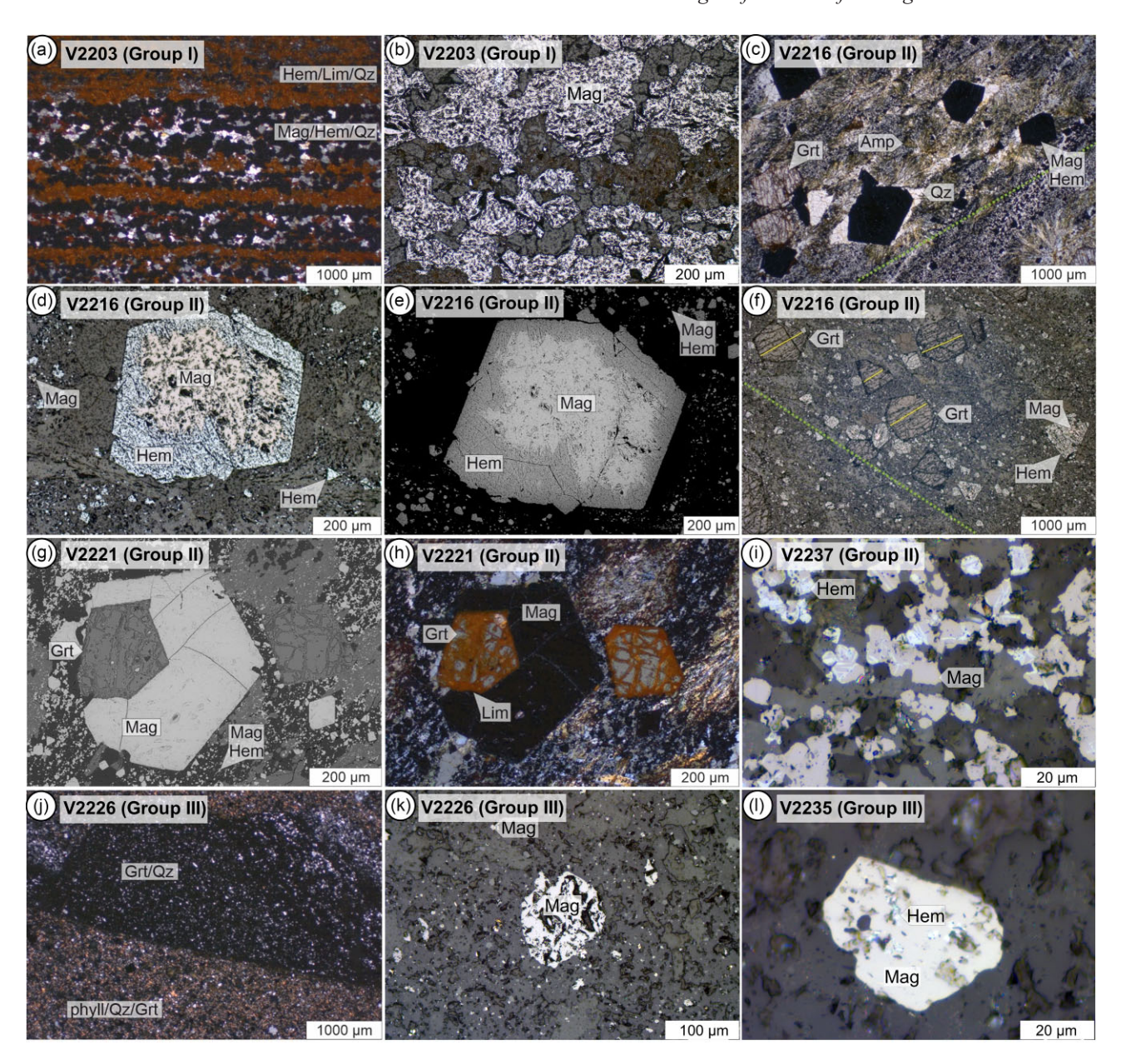


Figure 8. Microscopic images of Vredefort collar samples divided into three groups: (a, b) Group I, (c-i) Group II and (j-l) Group III. (a) Alternating layers of hematite (Hem), limonite (Lim), quartz (Qz) and magnetite (Mag); reflected light and crossed polarizers. (b) Magnetite grains; reflected polarized light. (c) Magnetite and hematite with strain shadows comprising quartz in the foliation plane (green dashed line) within a matrix of fine-grained quartz, coarse amphibole (Amp) and fractured garnet (Grt); transmitted polarized light. (d, e) Coarse-grained, euhedral magnetite rimmed by hematite; matrix composed of fine-grained magnetite and hematite; (d) reflected polarized light; (e) backscattered electron (BSE) image of (d). (f) Coarse garnet shows parallel fractures (yellow lines) near-perpendicular to the foliation plane (green dashed line) and occurs together with coarse magnetite and hematite in the fine-grained matrix; reflected polarized light. (g, h) Garnet included in magnetite with parallel crystal faces. Note the fine-grained magnetite/hematite in the matrix; (g) BSE image and (h) reflected light with crossed polarizers. (i) Euhedral magnetite and hematite; reflected polarized light. (j) Fine-grained matrix consisting of phyllosilicates (phyll), quartz, and garnet with a clast (dark) consisting of garnet and quartz; transmitted light with crossed polarizers. (k) Coarse and fine-grained magnetite; reflected polarized light. (l) Magnetite with hematite intergrowths; reflected polarized light.

Site S03 stands out for preserving coherent magnetization directions (Figs 5f–i and 6c), displaying lower NRM intensities (<25.3 A m<sup>-1</sup>) and higher MDF values (median of 40 mT) (Table 1), and experiencing minimal lightning remagnetization (Table 2). Differences in magnetization directions among the four blocks from site S03 can likely be explained by the proportion of SD grains in the

samples (Fig. 7a)—those from block #4 contain the highest proportion of SD grains and carry the paleomagnetic direction most resembling the 2.02 Ga direction right after impact (Fig. 6c). Although minor displacement of the blocks since remanence acquisition cannot be discounted for the other three blocks, that they are richer in multidomain grains makes them more susceptible to present-day field overprinting and/or lightning remagnetization. Carporzen *et al.* (2012) found that the magnetic signatures of granitoid rocks lying

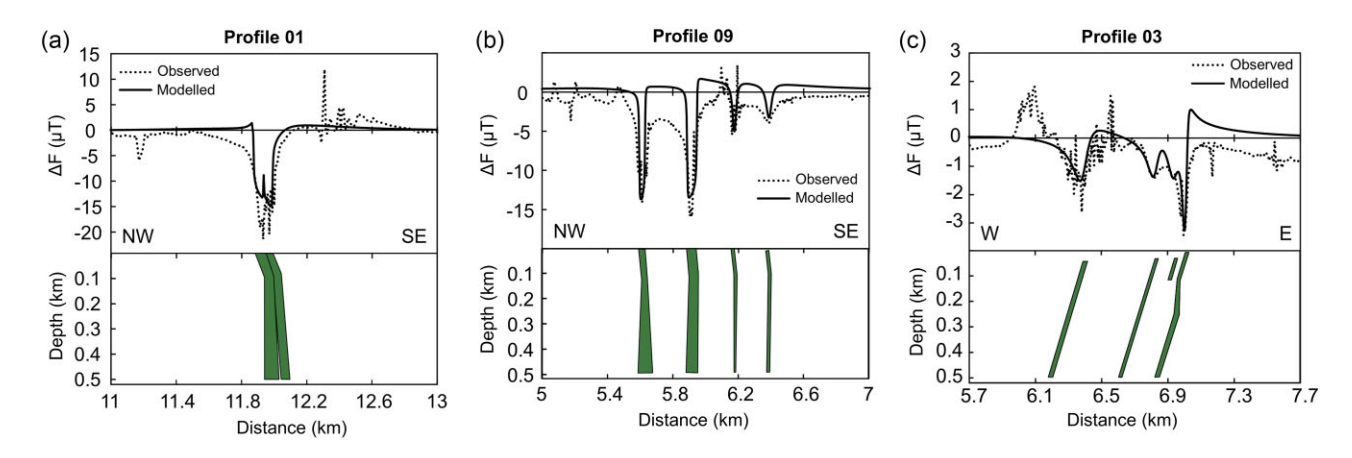


Figure 9. Modelling results for three ground magnetic profiles: (a) 01, (b) 09 and (c) 03. (top row) Comparison between observed and modelled magnetic field anomaly signals along profiles. (bottom row) Modelled magnetized bodies using the following parameters: 2.5-D magnetic sources, magnetization intensity 32.5 A  $\rm m^{-1}$ , inclination 57.2° and declination 25°.

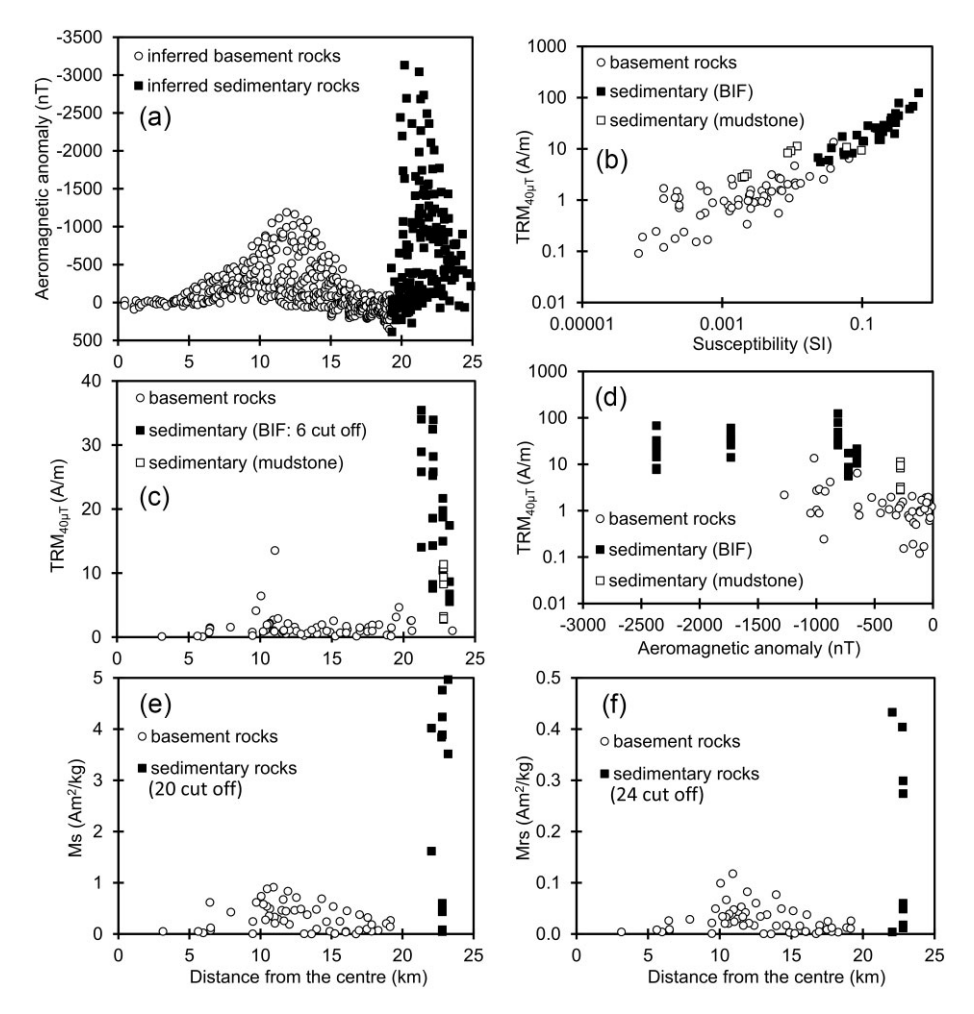


Figure 10. Comparison of the magnetic properties of basement core (circle symbols) and sedimentary collar rocks (square symbols) with aeromagnetic data. (a) Averaged aeromagnetic data along the radius from the centre of the Vredefort Dome towards the sedimentary collar. (b) Thermal remanent magnetization (TRM<sub>40</sub>) of the samples acquired in an applied magnetic field of 40  $\mu$ T versus bulk magnetic susceptibility (X<sub>40</sub>) of the samples measured after TRM<sub>40</sub> acquisition. (c) TRM<sub>40</sub> intensity as a function of distance from the centre of the Vredefort structure. (d) TRM<sub>40</sub> intensity versus corresponding ground magnetic anomaly amplitude near the sampling site. (e and f) Saturation magnetization (Ms) and remanent saturation magnetization (Mrs) as functions of distance from the centre of the structure (data from Carporzen 2006 and this study).

**Table 2.** Magnetic remanence values derived from stepwise AF demagnetization of NRM and TRM<sub>52 u.T</sub> for 13 sedimentary collar samples from the Vredefort Dome.

Sample	Site	$NRM (A m^{-1})$	$TRM_{52} (A m^{-1})$	$(NRM/TRM)_{20~mT}$	(NRM/TRM) <sup>norm</sup> <sub>20 mT</sub>	(NRM/TRM) <sub>25 mT</sub>	(NRM/TRM) <sup>norm</sup> 25 mT	(NRM/TRM) <sub>30 mT</sub>	(NRM/TRM) <sup>norm</sup> 30 mT
72202	S01	503.3	48.8	5.58	0.54	3.91	0.38	2.34	0.23
72211	S01	237.2	27.0	2.73	0.31	2.78	0.32	3.30	0.38
72216	60S	245.2	19.3	1.54	0.12	1.33	0.11	1.39	0.11
72237	90S	413.9	71.6	0.99	0.17	0.51	0.09	0.28	0.05
72239	90S	1033.0	111.3	1.97	0.21	1.27	0.14	0.90	0.10
V2244	S11	3.2	3.6	0.18	0.20	0.17	0.19	0.18	0.20
72247	S11	2.6	8.8	0.12	0.40	0.12	0.41	0.14	0.48
72255	808	130.0	28.3	2.78	0.61	2.41	0.53	2.26	0.49
72261	808	99.2	7.1	2.51	0.18	1.96	0.14	1.83	0.13
nedian		237.2	27.0	1.97	0.21	1.33	0.19	1.39	0.20
72228*	S03	15.8	16.2	1.01	1.04	0.95	0.97	0.82	0.84
72232*	S03	13.2	11.5	1.19	1.04	1.14	1.00	1.05	0.92
72233*	S03	3.8	4.2	0.92	1.00		1	98.0	0.94
72235*	S03	3.4	3.4	1.02	1.02	0.99	0.99	0.93	0.93
nedian		8.5	7.8	1.02	1.03	0.99	0.99	0.89	0.93

ratios of the NRM value after the 20, 25 and 30 mT AF steps divided by the TRM value after the 20, 25 and 30 mT AF steps, respectively; (NRM/TRM)<sub>20mT</sub>, (NRM/TRM)<sub>20mT</sub>, and (NRM/TRM)<sub>30mT</sub>, same as Abbreviations: NRM, natural remanent magnetization; TRM52, thermal remanent magnetization acquired in an applied magnetic field of 52  $\mu$ T; (NRM/TRM)<sub>20 mT</sub>, (NRM/TRM)<sub>25 mT</sub>, and (NRM/TRM)<sub>30 mT</sub>, above except that the NRM and TRM values were normalized by the initial values, \* indicate the samples (all from site S03) that are interpreted as being minimally affected by lightning-related overprinting. up to 10 m below the surface are influenced differentially by lightning, depending on the property considered (remanence direction, intensity, coercivity, etc.).

# 6.2. Thermoremanence acquisition shortly after impact

Stepwise AF demagnetization of samples from block #4 of site S03 isolates a linear component that decays univectorially to the origin on orthogonal projections, with a north-east and down direction of  $D = 46.3^{\circ}$ ,  $I = 54.4^{\circ}$ ,  $\alpha_{95} = 10.2^{\circ}$  (Fig. 6c), near the direction observed in the impact melts, with  $D = 25.0^{\circ}$ ,  $I = 57.2^{\circ}$ ,  $\alpha_{95} = 3.9^{\circ}$ (Carporzen et al. 2005). Moreover, stepwise AF and thermal demagnetization of the NRM of samples from site S03 mimic the behaviour when the same samples are given an artificial TRM and then stepwise demagnetized (Figs S2 and S3, Supporting Information). These observations indicate that at least a portion of the West Rand Group reached temperatures equal to or higher than the Curie temperature of magnetite (580 °C) prior to or during the impact and acquired thermoremanence shortly after the event, as inferred by Henkel & Reimold (2002). Although many surface rock samples from the sedimentary collar display high NRM intensities indicative of lightning-induced remagnetization, these shallow remanence effects are superimposed on longer-wavelength anomalies that reflect deeper, coherent remanent magnetizations.

The comparison of the magnetic properties of the paleomagnetic samples investigated in our study (metasediments) and the study by Carporzen *et al.* (2012) (basement rocks) with aeromagnetic data (Corner & Wilsher 1989) reveals that the absence of high-amplitude negative anomalies in the basement rocks proximal to the sediments, as well as those closer to the centre of the Vredefort Dome, can be attributed to lithologies depleted in magnetite (Fig. 10), as suggested by Hart *et al.* (1995) and Carporzen *et al.* (2005). TRM intensity peaks coincide with the peaks of aeromagnetic anomalies (Figs 10a and c), further supporting our hypothesis that the negative magnetic anomalies are due to the acquisition of a thermal remanence after impact and that the amplitude of the anomaly depends on magnetite concentration.

The presence of stable TRM and the absence of apparent shock effects in the investigated samples imply that pre-impact temperatures of the lower West Rand Group likely reached at least ~580 °C. This is higher than earlier estimates of 500–525 °C based on garnetbiotite thermometry of metapelites (Gibson et al. 1998). Assuming an elevated geothermal gradient of 30-40 °C km<sup>-1</sup>, related to the Bushveld metamorphic event (Gibson & Wallmach 1995), temperatures of ~580 °C correspond to pre-impact burial depths of approximately 14–19 km, consistent with both the present-day thickness of the collar sequence and the original stratigraphic thickness of the Witwatersrand basin (e.g. Phillips & Law 2000). This supports our interpretation that exhumation of already hot rocks accounted for the acquisition of thermoremanence in the Witwatersrand metasediments. However, numerical simulations by Ivanov (2005) suggest that the currently exposed collar rocks were originally overlain by hotter materials, including an impact melt sheet, that have since been eroded. These models indicate a post-impact thermal overprint of 50-100 °C above pre-impact conditions. Therefore, while exhumation alone was probably sufficient, we cannot exclude the possibility that thermal effects from the overlying impact melt also contributed to TRM acquisition, although the profiles in Figs 4(b) and (c) indicate that heating from above was negligible.

## 6.3. Identification of magnetic sources

The magnetic remanence intensity and direction of the rocks must be known to model the magnetic profiles; however, lightning strikes created abnormally deviatory NRMs in the surface samples. Therefore, the laboratory-imparted TRM intensity and remanence direction obtained from the granophyre dykes (Carporzen et al. 2005) were used in the forward magnetic modelling. The resulting models reflect signatures dominated by remanent magnetizations; indeed, explaining the intense negative anomalies via induced magnetization would be impossible. Modelling the negative anomalies with a TRM intensity of  $32.5 \text{ A m}^{-1}$  did not always match the amplitude of the anomalies (Profile 01: Fig. 9a), indicating that the actual source intensity could exceed 32.5 A m<sup>-1</sup> in places. The maximum measured TRM<sub>40</sub> intensity of 123.4 A m<sup>-1</sup> is more than sufficient to produce an intensity similar to the observed magnetic anomalies, but the signal shape remains difficult to fit. Modelling the anomalies required the creation of up to four magnetic bodies with thicknesses up to 70 m, spaced a maximum of 300 m apart. The good agreement between observed and modelled magnetic data supports the notion of a coherent magnetization vector throughout the Vredefort Dome. Residual mismatches between the observed data and our models likely arise due to uncertainties in the geometry of the source bodies and magnetite distribution within the bodies themselves (e.g. folding, faulting, or lithological heterogeneities were not accounted for in the models).

The modelled magnetic bodies correlate well with the known magnetic units from the lower West Rand Group (Fig. 4), as supported by microscopic observations. Based on mineralogy and microfabric, the investigated samples fall into three distinct groups (Fig. 8). Groups I and II are interpreted as metamorphosed banded iron formations (BIFs), given their abundance in magnetite and hematite, as well as their alternating quartz-rich and Fe-oxide-rich layers. In contrast, Group III contains magnetite only as an accessory phase within a matrix composed of phyllosilicate and quartz, consistent with a Fe-rich metapelite. Direct field investigations at the outcrops and the locations of the sampled sites on the geological map by Nel (1927) (Figs 2a and 4) suggest that sites S01, S04 and S06 correspond to the Water Tower Slates, while sites S08, S09 and S11 correspond to the Contorted Bed since they are located higher in stratigraphy. Site S03 lies in the lower part of the Brixton Formation, which might correspond to Blinkpoort magnetic mudstone (Fig. 4). Our findings provide the first direct identification of specific lithologies—the metamorphosed BIFs and magnetic mudstones within the Hospital Hill Subgroup of the West Rand Group as the main producers of the intensely negative magnetic anomalies in the Vredefort collar. The Water Tower Slates and the Contorted Bed were previously identified as magnetic markers elsewhere in the Witwatersrand Basin (Krahmann 1936; Smith et al. 2013). Our study confirms their lateral continuity and emphasizes their role as key remanence carriers. However, depending on the profile, the distance between the units varies from the generalized lithostratigraphic column, implying that the collar sequence is undoubtedly structurally more complex than currently known based on limited reflection seismic data and surface observations (e.g. Molezzi et al. 2019).

Curie temperature data and microscopic observations reveal the ubiquitous presence of magnetite in the BIF samples (Figs 7 and 8). Modelling the collar rocks with a pre-impact magnetic remanence, such as the Bushveld direction ( $D=175^{\circ}$ ,  $I=-62^{\circ}$ , Letts *et al.* 2009), after reorienting the strata from horizontal, fails to match the observed magnetic profiles (Fig. S7, Supporting Information);

whereas, modelling with the Vredefort remanence direction in the present-day folded configuration does (Fig. 9). The forward modelling results indicate that the iron formations producing the intense negative magnetic anomalies were deformed during the 2.02 Ga Vredefort event and acquired a thermoremanence shortly afterwards when the Earth's magnetic field was in a reversed polarity state.

Previous models of the magnetic anomalies in the Vredefort collar (Jackson 1982; Henkel & Reimold 1998, 2002) relied exclusively on aeromagnetic data and assumed broad, coherently magnetized rock bodies with remanence directions similar to those of the impact-generated granophyre dykes. Jackson (1982) modelled two overturned, ~500-m-wide magnetic sources with remanent magnetization intensities of 8 A m<sup>-1</sup> within the Witwatersrand sediments. Henkel & Reimold (2002) proposed models incorporating several magnetic sources with Q-values of 1.5 located within both the Witwatersrand and Ventersdorp Supergroups, without identifying the specific lithologies involved. These attempts to model the aeromagnetic data were unable to resolve the spatial relationships between the anomalies and geological units at a finer scale. Ground magnetic surveys conducted in the basement core of the Vredefort Dome (Muundjua et al. 2007; Fourie et al. 2019, 2023; Clark et al. 2021) have demonstrated the value of higher-resolution data in revealing structural and lithological details. Continuing in this vein, our highresolution ground magnetic data in the Vredefort collar, in combination with targeted sampling and rock magnetic and microfabric analyses, enabled the development of a more refined and lithologyspecific model. We show that the strongest magnetic anomalies in the collar originate from specific, narrow, steeply dipping BIFs and magnetic mudstones at the base of the Witwatersrand Supergroup units that had not previously been characterized in such detail within the Vredefort structure.

# 6.4. Metamorphism and the magnetization history of the collar BIFs

Understanding the origin of the intensely negative magnetic anomalies in the Vredefort Dome requires reconstructing the thermal and magnetic history of the BIFs and magnetic mudstones within the West Rand Group. These units record a complex history, including primary deposition, pre-impact regional metamorphism, impact-related structural deformation, post-impact cooling, and near-surface lightning-induced overprinting, as schematically shown in Fig. 11.

The BIFs were deposited between ~2.9 and 2.7 Ga in a marine environment as part of the lower Witwatersrand Supergroup (Frimmel 1996; Smith *et al.* 2013) and likely acquired a depositional remanent magnetization (Fig. 11a). Regional metamorphism occurred during the emplacement of the Bushveld Complex at 2.05–2.06 Ga, when the Witwatersrand strata experienced elevated geothermal gradients (~40 °C km<sup>-1</sup>; Gibson & Wallmach 1995) and reached greenschist to amphibolite facies conditions (~400–600 °C; Bisschoff 1982; Schreyer 1983; Gibson & Stevens 1998) (Fig. 11b). This event led to the crystallization of mm-sized magnetite and garnet in the BIFs at temperatures exceeding the Curie temperature of magnetite (580 °C).

The most intense metamorphism within the sedimentary collar is observed in the vicinity of the Schurwedraai alkaline-granite body (Figs 2a and 11b), which intruded the Witwatersrand rocks during the Bushveld magmatic event and developed a contact metamorphic aureole in the NNW sector of the structure (Bisschoff 1982; Martini 1992; Frimmel 1996; Graham *et al.* 2005). Hargraves (1970)

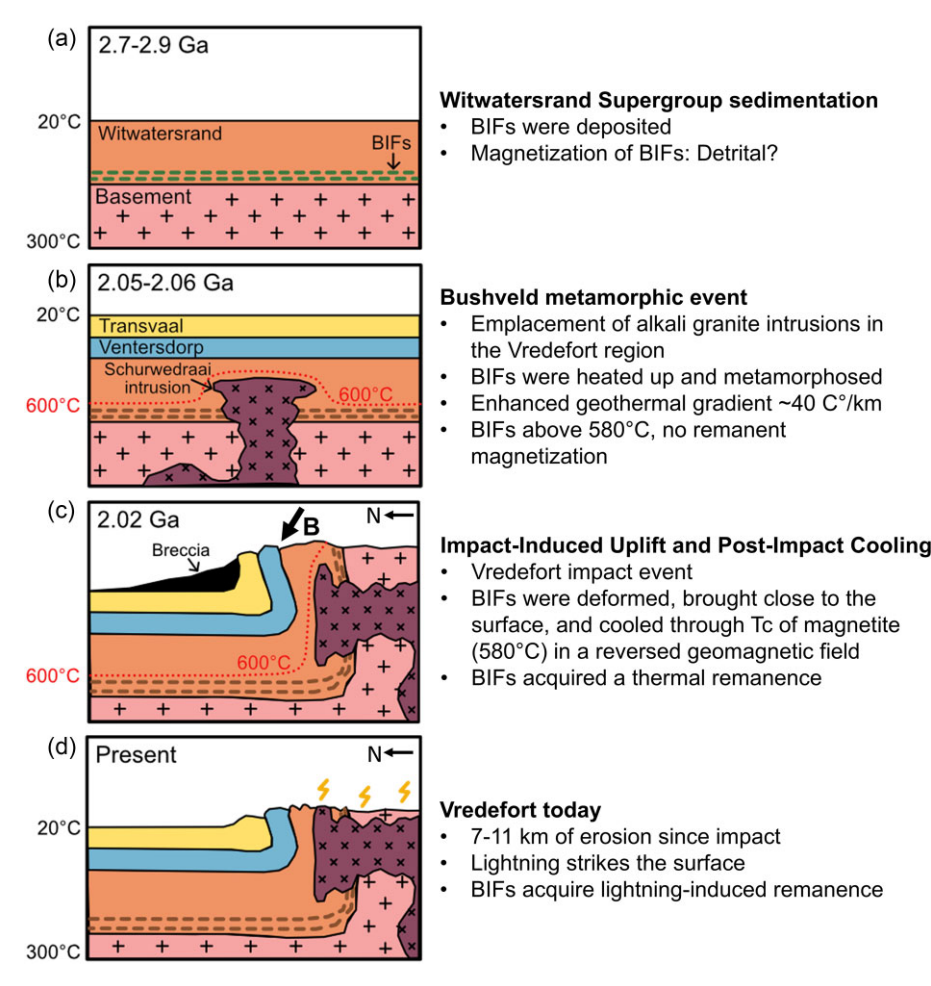


Figure 11. Schematic illustrations depicting major (re-)magnetization events recorded by the BIFs in the Vredefort collar: (a) primary deposition, (b) pre-impact regional metamorphism, (c) impact-related processes and (d) post-impact processes.

obtained widely scattered paleomagnetic results from the Schurwedraai pluton, noting that its average remanence direction is close to that of the granophyre dykes. Graham et al. (2005) suggested that the Schurwedraai body partially contributed to the steep pre-impact geothermal gradient reported by Gibson & Wallmach (1995) at the time of impact. Analyses of the ground magnetic data revealed that the most prominent negative anomalies are concentrated in this area (Fig. 2b and Table 1). Furthermore, the intensity of the magnetic anomalies diminishes with increasing distance from the collar-core contact (Fig. 4), which corresponds to the decreasing grade of metamorphism with shallower depth as well as lower temperatures approaching the pre-impact paleosurface. Positive anomalies in the southeastern sector could arise if the exhumation in the south was much less than in the north, to the absence of a Bushveld thermal pulse in the south, and/or if the beds are relatively flat-lying.

The Vredefort impact event (2.02 Ga) radically modified the thermal configuration of the region and caused significant structural disruption, including rapid exhumation of the central uplift, as well as folding and overturning of the metasedimentary collar strata (Fig. 11c). The BIFs were rapidly exhumed to shallower crustal levels. Shortly afterwards, they cooled through the Curie temperature of magnetite in the presence of a reversed geomagnetic field and acquired a TRM in their post-impact structural attitude as presently observed. This TRM is the primary source of

the observed negative magnetic anomalies in the Vredefort collar. Over the following two billion years, 7–11 km of erosion exposed the currently visible collar metasediments (Schreyer 1983; Gibson *et al.* 1998), which then became subject to lightning-induced remanent magnetization (LIRM; Fig. 11d). LIRM often overprints the original TRM at many sites, complicating the magnetic record.

## 7. CONCLUSIONS

Through high-resolution ground-based magnetic surveying, pale-omagnetic and microfabric analyses and magnetic modelling, we identified the key geological factors responsible for the distinct ring-shaped negative anomalies observed in the sedimentary collar of the Vredefort Dome. The most significant negative anomalies lay within 2 km near the contact between the sedimentary collar and the basement core. Anomaly amplitudes decrease with stratigraphic height and lie exclusively within the Hospital Hill Subgroup of the Witwatersrand Supergroup. Our magnetic modelling and TRM experiments show that the measured ground magnetic profiles can be explained by remanent magnetization intensities equal to or higher than 32.5 A m<sup>-1</sup> with the magnetization direction acting at Vredefort during impact. The remaining mismatches between the observed data and our models are likely due to imprecise knowledge of

the geometry of the source bodies and inhomogeneities in magnetite concentration.

We conclude that the pronounced negative magnetic anomalies in the Vredefort collar are primarily caused by specific banded iron formations, namely the Contorted Bed and Water Tower Slates from the Lower Witwatersrand Supergroup, that were uplifted and tilted due to the 2.02 Ga Vredefort impact event. The presence of a remanence direction closely matching that of impact-generated granophyre dykes supports the hypothesis that the rocks acquired a thermoremanent magnetization upon rapid cooling through the Curie temperature of magnetite from impact-induced uplift. This implies that the collar rocks of the Lower Witwatersrand Supergroup had temperatures of at least 580 °C prior to impact. Although high NRM intensities observed in most surface samples collected from the iron formations indicate lightning-induced remagnetization, these shallow remanence effects are superimposed on longerwavelength anomalies that reflect deeper, coherent remanent magnetizations.

Laboratory TRM experiments on basement rock samples, together with magnetic hysteresis and susceptibility data, indicate that the amplitude of the negative anomalies correlates with magnetite concentration. Lack of high-amplitude, negative anomalies in the basement rocks proximal to the sediments and those closer to the centre of the structure is attributed to lithologies impoverished in magnetite. Moving forward, obtaining more robust paleomagnetic directions in the collar rocks, unaffected by lightning, through approaches such as the Winkie-drill method (Carporzen et al. 2012) or sampling in underground mines would enhance the accuracy of our findings. Further structural analyses, high-resolution seismic image processing, and detailed geological mapping of the collar rocks are necessary to better constrain the geometry and distribution of magnetic units within the Vredefort collar.

#### SUPPORTING INFORMATION

Supplementary data are available at *GJIRAS* online.

Please note: Oxford University Press are not responsible for the content or functionality of any supporting materials supplied by the authors. Any queries (other than missing material) should be directed to the corresponding author for the article.

# ACKNOWLEDGMENTS

We acknowledge financial support from the Deutsche Forschungsgemeinschaft GI712/20–1 and TR534/9–1. Laurent Carporzen's PhD thesis provided the necessary guidance to make this study possible. We thank Armand Galdéano and Rodger J. Hart for their invaluable help during the ground magnetic survey and for their good nature, patience and support. We thank the reviewers, Matthew S. Huber and anonymous, and the editor, Eduard Petrovsky, for their insightful and helpful suggestions that improved our work.

#### DATA AVAILABILITY

Stepwise demagnetization and rock magnetic data are available on the MagIC portal: https://earthref.org/MagIC/20257. Ground magnetic data, modelling results, and Raman and EDS data can be accessed at: https://doi.org/10.5282/ubm/data.553. These data sets can also be obtained from the first two authors (iu.sleptsova@lmu.de and gilder@lmu.de).

#### REFERENCES

- Alken, P. et al., 2021. International geomagnetic reference field: the thirteenth generation, Earth Planets Space, 73, 49.
- Allen, N.H., Nakajima, M., Wünnemann, K., Helhoski, S. & Trail, D., 2022.
  A revision of the formation conditions of the Vredefort crater, J. Geophys.
  Res. Planets, 127, e2022JE007186.
- Antoine, L.A.G., Nicolaysen, L.O. & Niccol, S.L., 1990. Processed and enhanced gravity and magnetic images over the Vredefort structure and their interpretation, *Tectonophysics*, 171, 63–74.
- Armstrong, R.A., Compston, W., Retief, E., Williams, I.S. & Welke, H.J., 1991. Zircon ion microprobe studies bearing on the age and evolution of the Witwatersrand triad, *Precambrian Res.*, **53**, 243–266.
- Beaton, K.J., Gibson, R.L., Bybee, G.M., Walker, S., Diener, J.F.A. & Baxter, E.F., 2022. Amphibolite facies metamorphism in lower Witwatersrand Supergroup rocks exposed in the Vredefort Dome—a Ventersdorp LIP connection, S. Afr. J. Geol., 125, 191–210.
- Beukes, N.J., Guy, B.M. & Thiele, S.T., 2024. Stratigraphy and basin analysis of the West Rand Group, Witwatersrand Supergroup, *S. Afr. J. Geol.*, 127(2), 239–270.
- Bisschoff, A.A., 1969, The petrology of the igneous and metamorphic rocks in the Vredefort Dome and the adjoining parts of the Potchefstroom syncline, *D.Sc. thesis*, Univ. Potchefstroom.
- Bisschoff, A.A., 1972. Tholeitic intrusion in the Vredefort Dome, *Trans. Geol. Soc. S. Afr.*, **75**, 23–30.
- Bisschoff, A.A., 1982. Thermal metamorphism in the Vredefort Dome, *Trans. Geol. Soc. S. Afr.*, **85**, 43–57.
- Bisschoff, A.A., 1988. The history and origin of the Vredefort Dome, *S. Afr. J. Sci.*, **84**, 413–417.
- Bisschoff, A.A., 2000. The Geology of the Vredefort Dome (Explanation of Geological Sheets 2627CA, CB, CC, CD, DA, DC, and 2727 AA, AB, BA, 1: 50000 scale), Geological Survey of South Africa, pp. 49, Council for Geoscience. Pretoria.
- Brink, M.C., Waanders, F.B. & Bisschoff, A.A., 1997. Vredefort: a model for the anatomy of an astrobleme, *Tectonophysics*, 270, 83–114.
- Carporzen, L., 2006. Magnétisme des cratères d'impact de météorite à Vredefort (Afrique du Sud) et Rochechouart (France), *PhD thesis*, IPGP.
- Carporzen, L., Gilder, S.A. & Hart, R.J., 2005. Palaeomagnetism of the Vredefort meteorite crater and implications for craters on Mars, *Nature*, 435, 198–201.
- Carporzen, L., Weiss, B.P., Gilder, S.A., Pommier, A. & Hart, R.J., 2012. Lightning remagnetization of the Vredefort impact crater: no evidence for impact-generated magnetic fields, *J. geophys. Res.*, 117, E01007
- Christian, H.J. et al., 2003. Global frequency and distribution of lightning as observed from space by the Optical Transient Detector, J. geophys. Res., 108(D1), 4005.
- Clark, M.D., Kovaleva, E., Huber, M.S., Fourie, F. & Harris, C., 2021. Post-impact faulting of the Holfontein granophyre dike of the Vredefort impact structure, South Africa, inferred from remote sensing, geophysics, and geochemistry, *Geosciences*, 11(2), 96.
- Clendenin, C.W., Charlesworth, E.G. & Maske, S., 1988. Tectonic style and mechanism of Early Proterozoic successor basin development, Southern Africa, *Tectonophysics*, 156, 275–291.
- Corner, B., Durrheim, R.J. & Nicolaysen, L.O., 1990. Relationships between Vredefort structure and the Witwatersrand basin within tectonic framework of Kaapvaal craton as interpreted from regional gravity and aeromagnetic data, *Tectonophysics*, 171, 49–61.
- Corner, B. & Wilsher, W.A., 1989. Structure of the Witwatersrand Basin derived from interpretation of aeromagnetic and gravity data, in Proceedings of Exploration'87: Third Decennial International Conference on Geophysical and Geochemical Exploration for Minerals and Groundwater, Special Vol. 3, pp. 532–546, ed. Garland, G. D., Ontario Geological Survey.
- Day, R., Fuller, M. & Schmidt, V.A., 1977. Hysteresis properties of titanomagnetites: grain-size and compositional dependence, *Phys. Earth planet. Inter.*, 13, 4, 260–267.

- Dellefant, F., Trepmann, C.A., Gilder, S.A., Sleptsova, I.V., Kaliwoda, M. & Weiss, B.P., 2022. Ilmenite and magnetite microfabrics in shocked gneisses from the Vredefort impact structure, South Africa, Contrib. Mineral. Petrol., 177, 88.
- Dunlop, D.J., 2002. Theory and application of the Day plot (Mrs/Ms versus Hcr/Hc), 1. Theoretical curves and tests using titanomagnetite data, J. geophys. Res., 107(B3), 2056.
- Fisher, R., 1953. Dispersion on a sphere, Proc. R. Soc. Lond. A. Math. Phys. Sci., 217(1130), 295–305.
- Fourie, B., Huber, M.S. & Kovaleva, E., 2019. Geophysical characterization of the Daskop granophyre dyke and surrounding host rocks, Vredefort impact structure, South Africa, *Meteorit. Planet. Sci.*, 54(7), 1579–1593
- Fourie, B., Huber, M.S., Kovaleva, E. & Clark, M.D., 2023. Shallow depth extent of the Lesutoskraal granophyre dike in the Vredefort impact structure: geophysical surveys and trenching data, *Meteorit. Planet. Sci.*, 58(9), 1345–1364.
- Frimmel, H.E., 1996. Witwatersrand iron-formations and their significance for gold genesis and the composition limits of orthoamphibole, *Mineral. Petrol.*, **56**, 273–295.
- Gibert, D. & Galdeano, A., 1985. A computer program to perform transformations of gravimetric and aeromagnetic surveys, *Comp. Geosci.*, 11, 553–588
- Gibson, R.L., 1993. When is a hornfels not a hornfels? Metapelitic rocks from the lower Witwatersrand Supergroup, Vredefort Dome, South Africa, S. Afr. J. Geol., 96, 42–48.
- Gibson, R.L. & Reimold, W.U., 2005. Shock pressure distribution in the Vredefort impact structure, South Africa, in *Large Meteorite Impacts III*, Vol. 384, pp. 329–349, eds, Kenkmann, T., Hörz, F. & Deutsch, A., Geological Society of America.
- Gibson, R.L., Reimold, W.U., Phillips, D. & Layer, P.W., 2000. <sup>40</sup>Ar/<sup>39</sup>Ar constraints on the age of metamorphism in the Witwatersrand Supergroup, Vredefort dome (South Africa), S. Afr. J. Geol., 103(3-4), 175–190.
- Gibson, R.L., Reimold, W.U. & Stevens, G., 1998. Thermal-metamorphic signature of an impact event in the Vredefort dome, South Africa, *Geology*, 26, 787–790.
- Gibson, R.L. & Stevens, G., 1998. Regional metamorphism due to anorogenic intracratonic magmatism, Geol. Soc. Spec. Publ., 138, 121–135.
- Gibson, R.L. & Wallmach, T., 1995. Low pressure-high temperature metamorphism in the Vredefort Dome, South Africa: anticlockwise pressuretemperature path followed by rapid decompression, Geol. J., 30, 319–331.
- Gijben, M., 2012. The lightning climatology of South Africa, S. Afr. J. Sci., 108(3/4), 10.
- Graham, I.T., De Waal, S.A. & Armstrong, R.A., 2005. New U-Pb SHRIMP zircon age for the Schurwedraai alkali granite: implications for pre-impact development of the Vredefort Dome and extent of Bushveld magmatism, South Africa, J. Afr. Earth Sci., 43, 537–548.
- Grieve, R. & Therriault, A., 2000. Vredefort, Sudbury, Chiexulub: three of a Kind?, Ann. Rev. Earth planet. Sci., 28, 305–338.
- Guy, B.M., Beukes, N.J. & Gutzmer, J., 2010. Palaeoenvironmental controls on the textures and chemical composition of pyrite from non-conglomeritic sedimentary rocks of the Mesoarchaean Witwatersrand Supergroup, South Africa, S. Afr. J. Geol., 113(2), 195–228.
- Hargraves, R.B., 1970. Paleomagnetic evidence relevant to the origin of the Vredefort ring, J. Geol., 78, 253–263.
- Hart, R.J., Andreoli, M.A.G., Smith, C.B., Otter, M.L. & Durrheim, R., 1990b. Ultramafic rocks in the centre of the Vredefort structure: possible exposure of the upper mantle?, *Chem. Geol.*, 83, 233–248.
- Hart, R.J., Andreoli, M.A.G., Tredoux, M. & Wit, M.J., 1990a. Geochemistry across an exposed section of Archean crust at Vredefort, South Africa: with implications for mid-crustal discontinuities, Chem. Geol., 82, 21–50.
- Hart, R.J., Connell, S.H., Cloete, M., Mare, L., Drury, M. & Tredoux, M., 2000. "Super magnetic" rocks generated by shock metamorphism from the centre of the Vredefort impact structure, South Africa, S. Afr. J. Geol., 103, 151–155.
- Hart, R.J., Hargraves, R.B., Andreoli, M.A.G., Tredoux, M. & Doucouré, C.M., 1995. Magnetic anomaly near the center of the Vredefort structure:

- implications for impact-related magnetic signatures, *Geology*, **23**, 277–280.
- Hart, R.J., McDonald, I., Tredoux, M., de Wit, M.J., Carlson, R.W., Andreoli, M., Moser, D.E. & Ashwal, L.D., 2004. New PGE and Re/Os-isotope data from lower crustal sections of the Vredefort dome and a reinterpretation of its "crust on edge" profile, S. Afr. J. Geol., 107, 173–184.
- Hart, R.J., Welke, H.J. & Nicolaysen, L.O., 1981. Geochronology of the deep profile through Archean basement at Vredefort, with implications for early crustal evolution, *J. Geophys. Res. Solid Earth*, 86(B11), 10 663– 10 680
- Henkel, H. & Reimold, W.U., 1998. Integrated geophysical modelling of a giant, complex impact structure: anatomy of the Vredefort Structure, South Africa, *Tectonophysics*, 287, 1–20.
- Henkel, H. & Reimold, W.U., 2002. Magnetic model of the central uplift of the Vredefort impact structure, South Africa, J. Appl. Geophys., 51, 43–62.
- Huber, M.S., Kovaleva, E., Clark, M.D., Riller, U. & Fourie, F.D., 2022. Evidence from the Vredefort Granophyre Dikes points to crustal relaxation following basin-size impact cratering, *Icarus*, 374, 114812.
- Huber, M.S., Kovaleva, E., Rae, A.S.P., Tisato, N. & Gulick, S.P.S., 2023.
  Can Archean impact structures be discovered? A case study from Earth's largest, most deeply eroded impact structure, *J. Geophys. Res. Planets*, 128, e2022JE007721.
- Ivanov, B.A., 2005. Numerical modeling of the largest terrestrial meteorite craters, Sol. Syst. Res., 39(5), 381–409.
- Jackson, G.M., 1982. Paleomagnetic study and magnetic modeling of the Vredefort dome, B.Sc. honors. thesis, Univ. Witwatersrand.
- Jahn, A. & Riller, U., 2009. A 3D model of first-order structural elements of the Vredefort Dome, South Africa-Importance for understanding central uplift formation of large impact structures, *Tectonophysics*, 478, 221–229.
- Jones, C.H., 2012. Updaters for GravMag, Available at:http://cires1.colorad o.edu/people/jones.craig/GSSH/index.html( accessed March 8, 2024).
- Kamo, S.L., Reimold, W.U., Krogh, T.E. & Colliston, W.P., 1996. A 2.023 Ga age for the Vredefort impact event and a first report of shock metamorphosed zircons in pseudotachylitic breccias and granophyre, *Earth planet. Sci. Lett.*, 144, 369–387.
- Kaub, L., Wack, M.R. & Gilder, S., 2023. SushiBar2.0: an upgraded, fully automated paleo- and rock magnetic measurement system in Munich, AGU Fall Meeting Abstracts, GP41B–0506, American Geophysical Union.
- Kirschvink, J., 1980. The least-squares line and plane and the analysis of palaeomagnetic data, Geophys. J. Int., 62(3), 699–718.
- Koeberl, C., Reimold, W.U. & Shirey, S.B., 1996. Re-Os isotope and geochemical study of the Vredefort Granophyre: clues to the origin of the Vredefort structure, South Africa, Geology, 24, 913–916.
- Koenigsberger, J.G., 1938. Natural residual magnetism of eruptive rocks, *Terr. Mag. Atmos. Electr.*, **43**, 119–130.
- Krahmann, R., 1936. The geophysical magnetometric investigations on West Witwatersrand areas between Randfontein and Potchefstroom, Transvaal, J. South. Afr. Inst. Min. Metall., 36(9), 247–279.
- Lana, C., Gibson, R.L., Kisters, A.F.M. & Reimold, W.U., 2003a. Archean crustal structure of the Kaapvaal craton, South Africa—evidence from the Vredefort dome, *Earth planet. Sci. Lett.*, 206(1–2), 133–144.
- Lana, C., Reimold, W.U., Gibson, R.L., Koeberl, C. & Siegesmund, S., 2004.
  Nature of the Archean midcrust in the core of the Vredefort Dome, Central Kaapvaal Craton, South Africa, *Geochim. Cosmochim. Acta*, 68(3), 623–642..
- Lana, C.E., Gibson, R.L. & Reimold, W.U., 2003b. Impact tectonics in the core of the Vredefort dome, South Africa: implications for central uplift formation in very large impact structures, *Meteorit. Planet. Sci.*, 38, 1093–1107
- Letts, S., Torsvik, T.H., Webb, S.J. & Ashwal, L.D., 2009. Palaeomagnetism of the 2054 Ma Bushveld Complex (South Africa): implications for emplacement and cooling, *Geophys. J. Int.*, 179, 850–872.
- Martini, J.E.J., 1992. The metamorphic history of the Vredefort dome at approximately 2 Ga as revealed by coesite-stishovite-bearing pseudotachylites, J. Metamorph. Geol., 10, 517–527.

- McCarthy, T.S., 2006. The Witwatersrand Supergroup, in *The geology of South Africa: Johannesburg*, pp. 155–186, eds, Johnson, M.R., Anhaeusser, C.R. & Thomas, R.J., Geological Society of South Africa.
- Molezzi, M.G., Hein, K.A.A. & Manzi, M.S.D., 2019. Mesoarchaean-Palaeoproterozoic crustal-scale tectonics of the central Witwatersrand basin—Interpretation from 2-D seismic data and 3-D geological modelling, *Tectonophysics*, 761, 65–85.
- Moser, D., Flowers, R.M. & Hart, R.J., 2001. Birth of the Kaapvaal tectosphere 3.08 billion years ago, *Science*, **291**(5503), 465–468.
- Moser, D.E., 1997. Dating the shock wave and thermal imprint of the giant Vredefort impact, South Africa, *Geology*, **25**, 7–10.
- Mücke, A. & Raphael Cabral, A., 2005. Redox and nonredox reactions of magnetite and hematite in rocks, *Chem. Erde*, 65, 271–278.
- Muundjua, M., Hart, R.J., Gilder, S.A., Carporzen, L. & Galdeano, A., 2007. Magnetic imaging of the Vredefort impact crater, South Africa, Earth planet. Sci. Lett., 261, 456–468.
- Nel, L.T., 1927. Geological map of the country around Vredefort, scale 1:63360, Union of South Africa, Department of Mines and Industries, Geological Survey, Council for Geoscience, Pretoria.
- Pedley, R.C., Busby, J.P. & Dabek, Z.K., 1993. GRAVMAG User Manual Interactive 2.5D Gravity and Magnetic Modelling, pp. 73, British Geological Survey, Technical Report WK/93/26/R, Nottingham.
- Phillips, G.N. & Law, J.D.M., 2000. Witwatersrand gold fields: geology, genesis and exploration, Rev. Econ. Geol., 13, 439–500.
- Reimold, W.U. et al. 2023. Genesis of the mafic impact melt rock in the northwest sector of the Vredefort Dome, South Africa, Meteorit. Planet. Sci., 58, 907–944.
- Reimold, W.U. & Gibson, R.L., 2006. The melt rocks of the Vredefort impact structure—Vredefort granophyre and pseudotachylitic breccias: implications for impact cratering and the evolution of the Witwatersrand Basin, Chem. Erde, 66, 1–35.
- Roux, A.T., 1970. The application of geophysics to gold exploration in South Africa, in *Mining and groundwater geophysics/1967, Economic Geology Report No. 26*, pp. 425–438, ed., Morley, L.W., Geological Survey of Canada, Department of Energy, Mines and Resources, Ottawa, Canada.
- Salminen, J., Pesonen, L.J., Lahti, K. & Kannus, K. 2013. Lightning-induced remanent magnetization—the Vredefort impact structure, South Africa, *Geophys. J. Int.*, 195, 117–129.

- Schreyer, W., 1983. Metamorphism and fluid inclusions in the basement of the Vredefort Dome, South Africa: guidelines to the origin of the structure. J. Petrol., 24, 26–47.
- Smith, A.J.B., Beukes, N.J. & Gutzmer, J., 2013. The composition and depositional environments of Mesoarchean iron formations of the West Rand Group of the Witwatersrand Supergroup, South Africa, *Econ. Geol.*, 108, 111–134.
- Spray, J.G., Kelley, S.P. & Reimold, W.U., 1995. Laser probe argon-40/argon-39 dating of coesite- and stishovite-bearing pseudotachylytes and the age of the Vredefort impact event, *Meteorit. Planet. Sci.*, 30, 335–343.
- Stettler, E.H., Fourie, C.J.S., Bühmann, J.R., Hattingh, E., Cole, P., Kleywegt, R.J., Wolmarans, L.G. & Cloete, A.J., 1999. Magnetics. South African Geophysical Atlas. Volume 2 (CD Rom), Council for Geoscience, South Africa.
- Therriault, A.M., Grieve, R.A.F. & Reimold, W.U., 1997a. Original size of the Vredefort Structure: implications for the geological evolution of the Witwatersrand Basin, *Meteorit. Planet. Sci.*, 32, 71–77.
- Therriault, A.M., Reimold, W.U. & Reid, A.M., 1997b. Geochemistry and impact origin of the Vredefort granophyre, S. Afr. J. Geol., 100, 115–122.
- Tredoux, M., Hart, R.J., Carlson, R.W. & Shirey, S.B., 1999. Ultramafic rocks at the center of the Vredefort structure: further evidence for the crust on edge model, *Geology*, 27(10), 923–926.
- Tucker, R.F., Viljoen, R.P. & Viljoen, M.J., 2016. A review of the Witwater-srand Basin—The world's greatest goldfield, *Episodes*, **39**, 104–133.
- Turtle, E.P., Pierazzo, E. & O'Brien, D.P., 2003. Numerical modeling of impact heating and cooling of the Vredefort impact structure, *Meteorit. Planet. Sci.*, 38(2), 293–303.
- Wack, M. & Gilder, S., 2012. The SushiBar: an automated system for paleomagnetic investigations, Geochem. Geophys. Geosyst., 13(3).
- Walraven, F., 1997. Geochronology of the Rooiberg Group, 21pp., Transvaal Supergroup, South Africa, Economic Geology Research Unit, University of the Witwatersrand, Johannesburg, South Africa, Information Circular No. 316.
- Wassmann, S. & Stöckhert, B., 2013. Rheology of the plate interface—Dissolution precipitation creep in high pressure metamorphic rocks, *Tectonophysics*, **608**, 1–29.
- Wieland, F., Reimold, W.U. & Gibson, R.L., 2006. New observations on shatter cones in the Vredefort impact structure, South Africa, and evaluation of current hypotheses for shatter cone formation, *Meteorit. Planet. Sci.*, **41**(11), 1737–1759.